

To appear in ApJ

Spitzer IRS Spectra of Debris Disks in the Scorpius-Centaurus OB Association

Hannah Jang-Condell¹, Christine H. Chen², Tushar Mittal^{2,3}, P. Manoj⁴, Dan Watson⁵,
Carey M. Lisse^{2,6}, Erika Nesvold^{7,8}, Marc Kuchner⁷

ABSTRACT

We analyze Spitzer/IRS spectra of 110 B-, A-, F-, and G-type stars with optically thin infrared excess in the Scorpius-Centaurus (ScoCen) OB association. The age of these stars ranges from 11-17 Myr. We fit the infrared excesses observed in these sources by Spitzer/IRS and Spitzer/MIPS to simple dust models according to Mie theory. We find that nearly all the objects in our study can be fit by one or two belts of dust. Dust around lower mass stars appears to be closer in than around higher mass stars, particularly for the warm dust component in the two-belt systems, suggesting mass-dependent evolution of debris disks around young stars. For those objects with stellar companions, all dust distances are consistent with truncation of the debris disk by the binary companion. The gaps between several of the two-belt systems can place limits on the planets that might lie between the belts, potentially constraining the mass and locations of planets that may be forming around these stars.

Subject headings: open clusters and associations: individual (Upper Scorpius, Lower Centaurus-Crux, Upper Centaurus-Lupus)—stars: circumstellar matter—planetary systems: formation — planet-disk interactions

¹Department of Physics and Astronomy, University of Wyoming, Laramie, WY 82071

²Space Telescope Science Institute, 3700 San Martin Dr., Baltimore, MD 21218

³Department of Earth and Planetary Science, University of California, Berkeley, CA 94720

⁴Department of Astronomy & Astrophysics, Tata Institute of Fundamental Research, Homi Bhabha Rd, Mumbai 400005, India

⁵Department of Physics and Astronomy, University of Rochester, Rochester, NY 14627

⁶Johns Hopkins University Applied Physics Laboratory, Laurel, MD 20723

⁷NASA Goddard Space Flight Center, Greenbelt, MD

⁸University of Maryland Baltimore County, Baltimore, MD 21250

1. Introduction

High contrast imaging surveys using adaptive optics (AO) enabled large telescopes are beginning to discover Jovian planets in nascent planetary systems. These surveys typically target nearby (<100 pc), young (<300 Myr) stars because atmospheric modeling of Jovian planets predicts that their self-emission is bright when they are young and fades with time, because of their captured heat of formation and ongoing gravitational contraction (Marley et al. 2007). Debris disks are dusty disks around main sequence stars that are typically discovered via excess thermal infrared emission above the stellar photosphere. *Spitzer* MIPS surveys of young clusters and field stars indicate that young stars generally possess larger infrared excess than old stars (Su et al. 2006; Carpenter et al. 2009a). In fact, the first images of Jovian exoplanets were made in the dusty debris disk systems, HR 8799 (Marois et al. 2010) and β Pictoris (Lagrange et al. 2010). Mid- to far-infrared excess was originally discovered toward these targets more than two decades ago using the *IRAS* satellite (Aumann 1984; Backman & Paresce 1993).

Studies of the spatial distribution of dust in debris disks can provide constraints on the presence of planets. For example, SED modeling of the thermal emission from the dust around HR 8799 indicates the presence of two dust populations generated by two separate parent body belts, one interior to 10 AU and another beyond 100 AU (Su et al. 2009; Chen et al. 2009). The system of four $\sim 10 M_{Jup}$ planets discovered using the Keck Telescope lies between these two dust populations at distances of 15, 24, 38, and 68 AU (Marois et al. 2010). Similarly, SED modeling of *IRAS* excesses toward β Pictoris indicates that the dust is located at distances >20 AU (Backman & Paresce 1993) and the Jovian planet β Pic b lies inside the central clearing at 10 AU (Lagrange et al. 2010). SMA observations of β Pic have further revealed a ring of millimeter-sized grains at ~ 94 AU that has been identified as the location of the main reservoir of dust-producing planetesimals (Wilner et al. 2011). The architecture of the β Pic system is consistent with creation of dust by collisions among parent bodies in the main belt, the larger of which spiral inward under Poynting-Robertson drag until they encounter β Pic b and are scattered out of the system. A study of strong silicate emission at 8-13 μm of β Pic finds evidence for belts at 6, 16, and 30 AU (Okamoto et al. 2004). These belts may also be sculpted by β Pic b, and possibly additional as-yet-undiscovered planets. The infrared spectrum of the dust in β Pic support this picture (Chen et al. 2007). Stellar activity and starspots in young stars make the detection of planets by radial velocities and transits infeasible, especially in later type stars, meaning that direct imaging and gap characterization may be some of the best methods of finding planets in young stars, particularly in pre-main sequence stars.

Simple black body modeling of ~ 500 debris disks observed with the *Spitzer* IRS and

MIPS at 70 μm indicates that the excess from one-third of the targets can be described using a single temperature black body with a median grain temperature, $T_{gr} \sim 180$ K, and the excess from two-thirds of the targets can be described using a two temperature black body model with median grain temperatures, $T_{gr} \sim 80$ K and 340 K (Chen et al. 2014). In these systems, the presence of Jovian planets could naturally explain how planetesimals populations are (1) dynamically excited leading to collisions between parent bodies and (2) sculpted into rings. However, coagulation N-body simulations of 'self-stirred' disks suggest that significantly smaller Pluto-sized objects may also induce collisions between parent bodies (Kenyon & Bromley 2004). A detailed census of Jovian-mass planets in debris disks is needed to determine the role that Jovian planets play in exciting and sculpting parent body belts. Gemini South and VLT have recently commissioned GPI and SPHERE, second-generation coronagraphs, that are expected to take of census of planets with masses $>1 M_{Jup}$ around nearby, young stars (Macintosh et al. 2014).

Prime targets for these searches will be young stars in the Scorpius-Centaurus OB association (ScoCen). ScoCen is the closest OB association to the Sun with typical stellar distances of ~ 100 - 200 pc and contains three subgroups: Upper Scorpius (US), Upper Centaurus Lupus (UCL), and Lower Centaurus Crux (LCC), with estimated ages of ~ 11 Myr, ~ 15 Myr, and ~ 17 Myr, (Pecaut et al. 2012; Mamajek et al. 2002) respectively. Several hundred candidate members have been identified to date, although the association probably contains thousands of low-mass members. Member stars with spectral-type F and earlier have been identified using moving group analysis of *Hipparcos* positions, parallaxes, and proper motions (de Zeeuw et al. 1999), while later-type members have been identified using youth indicators (i.e., high coronal X-ray activity and large lithium abundance; (Preibisch & Mamajek 2008; Slesnick et al. 2006)). Jovian mass planets have already been discovered in two ScoCen debris disk systems thus far. VLT NaCO differential imaging at L'-band has revealed the presence of a $5.2 M_{Jup}$ planet at 56 AU (0.62'') from HD 95086, an A8V member of LCC (Rameau et al. 2013). Magellan AO + Clio2 differential imaging at J-, Ks- and L'-bands has revealed the presence of an $11 M_{Jup}$ planet at 650 AU from HD 106906, a F5 member of LCC (Bailey et al. 2014).

We report here the results of a study modeling the *Spitzer* IRS and MIPS 70 μm SEDs of all of the debris disks around B- through G-type ScoCen members observed during the *Spitzer* cryogenic mission. Our scientific goal is to better constrain the location of debris dust and infer the presence of planets and their orbital properties where possible. We list the targets for the sample, along with their spectral types, distances, and subgroup memberships in Table 1. For debris disks with two belts, the width of a gap between the belts can provide important constraints on the mass of a planet orbiting within the disk (Quillen 2006; Chiang et al. 2009). Nesvold & Kuchner (2014) used the 3D collisional debris

disk model SMACK to derive a relationship between gap width, planet mass, stellar age, and disk optical depth. We use this relationship to determine which of the two-belt ScoCen targets are consistent with a planet on a circular orbit, and which require multiple planets or eccentric planet orbits. For the systems consistent with a single non-eccentric planet, we place an upper limit on the mass of the putative perturbing planet.

2. Observations

The infrared properties of nearby, young stars in ScoCen were systematically explored during the *Spitzer* cryogenic mission. Observers used the MIPS mid-IR photometric camera to search for infrared excess at 24 and/or 70 μm around ScoCen members selected based on *Hipparcos* astrometry (de Zeeuw et al. 1999), color-magnitude diagrams Preibisch & Zinnecker (1999); Preibisch et al. (2002), and x-ray surveys (Walter et al. 1994; Martín 1998; Preibisch et al. 1998; Kunkel 1999; Köhler et al. 2000). They followed-up excess targets using the IRS mid-IR spectrometer at 5-35 μm to search for solid-state emission features and characterize the shapes of the SEDs. Taken together, the *Spitzer* MIPS photometry indicated that approximately one-quarter of the \sim 600 ScoCen stars observed using MIPS possess infrared excess (Su et al. 2006; Carpenter et al. 2009b; Chen et al. 2011, 2012). For stars with ages 10 - 20 Myr, stellar evolutionary models suggest that stars with spectral type earlier than F are main sequence while stars later than F are not. The infrared excess properties of late-type stars in Upper Sco are consistent with gas-rich, optically thick T Tauri stars while those of early-type stars in Upper Sco and early- and solar-type stars in UCL and LCC are consistent with gas-depleted, optically thin debris disks. Because our models are only valid for optically thin disks, we focus only on the debris disks.

The *Spitzer* IRS spectra for ScoCen members possess a diverse array of properties. For example, the spectrum of the F3/F5 LCC member HIP 63975 (HD 113766) shows prominent 10 and 20 μm silicate emission features consistent with the presence of forsterite, enstatite, olivine, and pyroxene-rich dust, generated by the destruction of a $\gtrsim 300$ km radius asteroid. Detailed modeling of the IRS spectrum suggests that the dust in this system is located in two cold belts located at 4 - 9 AU and 30 - 80 AU from the star, plus a warm belt at 1.8 AU (Lisse et al. 2008). By contrast, the IRS spectra of debris disks around B- and A-type stars in Upper Sco reveal rising continua without strong solid-state emission features. The dust in these systems has been modeled using a single temperature black body (Dahm & Carpenter 2009). We have collected all of the IRS spectra of ScoCen US, UCL, and LCC debris disks and analyzed their spectra self-consistently. In Figure 1, we plot the K_s -[24] color as a function of $J - H$ color (as a proxy for spectral type) for all of the sources observed using MIPS and

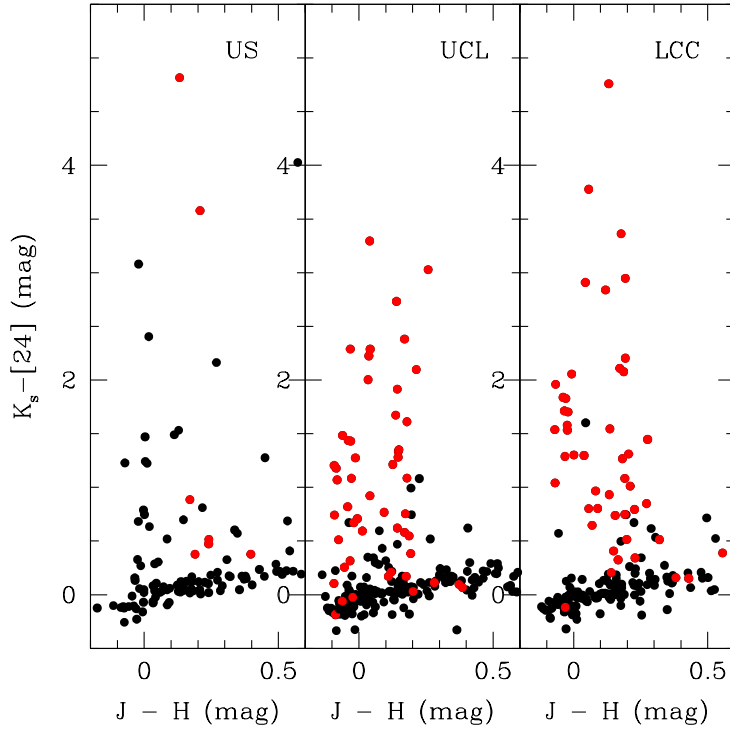


Fig. 1.— Color-color plot of all ScoCen targets surveyed with Spitzer. We plot in black all of the objects surveyed with MIPS (Su et al. 2006; Carpenter et al. 2008, 2009b; Chen et al. 2011, 2012), and in red the objects whose IRS spectra are studied here.

overlay the targets analyzed here in red. We note that the IRS spectra for 26 disk-bearing members of the \sim 11 Myr old Upper Sco have been modeled in detail by Dahm & Carpenter (2009); for self-consistency, we independently model the spectra of all of the debris disks in their sample but do not reanalyze those of the primordial disks. We further note that some MIPS UCL and LCC excess sources were not observed using the IRS.

We drew the calibrated IRS spectra for our targets from the *Spitzer* IRS Debris Disk Catalog (Chen et al. 2014). Calibrated IRS low-resolution spectra typically possess absolute calibration uncertainties of 5% while calibrated MIPS 24 μ m fluxes typically possess calibration uncertainties of 2% (Engelbracht et al. 2007). Therefore, the spectra in the Debris Disk catalog are pinned to the MIPS 24 μ m fluxes as reported in the *Spitzer* Enhanced Imaging Products (SEIP) Catalog¹ to improve the absolute calibration of the data. The IRS Debris Disk catalog contains not only the spectra for debris disks but also their re-

¹<http://irsa.ipac.caltech.edu/data/SPITZER/Enhanced/Imaging/overview.html>

peatability uncertainties, $\sigma_{\text{IRS},\lambda}$, estimated using the difference between spectra obtained at two separate nod positions. Since the repeatability uncertainty can vary substantially from pixel-to-pixel, inconsistent with our understanding of the instrument, we averaged the repeatability uncertainty in quadrature over the nearest 5 points with boxcar weighting to smooth out anomalously low or high values. To wit, if $\sigma_{0,i}$ is the IRS repeatability error at λ_i , then

$$\sigma_{\text{IRS},i}^2 = \sum_{j=i-2}^{i+2} \frac{\sigma_{0,i}^2}{5}. \quad (1)$$

One source, HIP 77911, was observed only at high resolution with IRS. For this source, we used the CASSIS (Cornell AtlaS of Spitzer/IRS Sources) optimal reduction of the data (Lebouteiller et al. 2011). The spectrum appears different from that of the other sources because the spectral resolution is higher and the wavelength coverage does not extend shortward of 10 microns.

We photosphere-subtracted our spectra using our own stellar photosphere models. For stars whose MIPS data were analyzed by Chen et al. (2011, 2012), we adopted stellar spectral types, effective temperatures (T_{eff}), visual extinctions (A_V), and luminosities (L_*) published therein. Stellar properties for sources not analyzed in these papers were taken from the references indicated in Table 1. Then, we selected Kurucz model atmospheres² (Kurucz 1979) consistent with the listed effective temperatures, assuming solar abundances and surface gravities, $\log g = 4.0$. Next, we reddened the stellar model SEDs assuming the Cardelli, Clayton, & Mathis interstellar extinction law and $A_V = 3.1E(B-V)$. Finally, we normalized these stellar atmospheres to the MIPS 24 μm predictions given by Chen et al. (2011, 2012), with the same 3% photosphere calibration error used in those works. The total uncertainty in the photosphere-subtracted spectrum is

$$\sigma_{\text{excess},\lambda} = \sqrt{\sigma_{\text{IRS},\lambda}^2 + \sigma_{\text{phot},\lambda}^2} \quad (2)$$

where $\sigma_{\text{phot}} = 3\% \times F_{\text{phot}}$. In Figures 2a-2e, we show the reduced and photosphere-subtracted spectra of our sources.

In Table 1, we summarize the stellar properties of the 119 Sco Cen members whose IRS spectra are discussed here. The distances to the sources are taken from Hipparcos measurements (van Leeuwen 2007). Of these sources, 5 are Be stars, and are not analyzed: HIP 63005, HIP 67472, HIP 69618, HIP 77859, and HIP 78207. Another 4 sources are optically thick protoplanetary disks: HIP 56354 (HD 100453), HIP 56379 (HD 100546), HIP

²<http://www.stsci.edu/hst/observatory/cdbs/k93models.html>

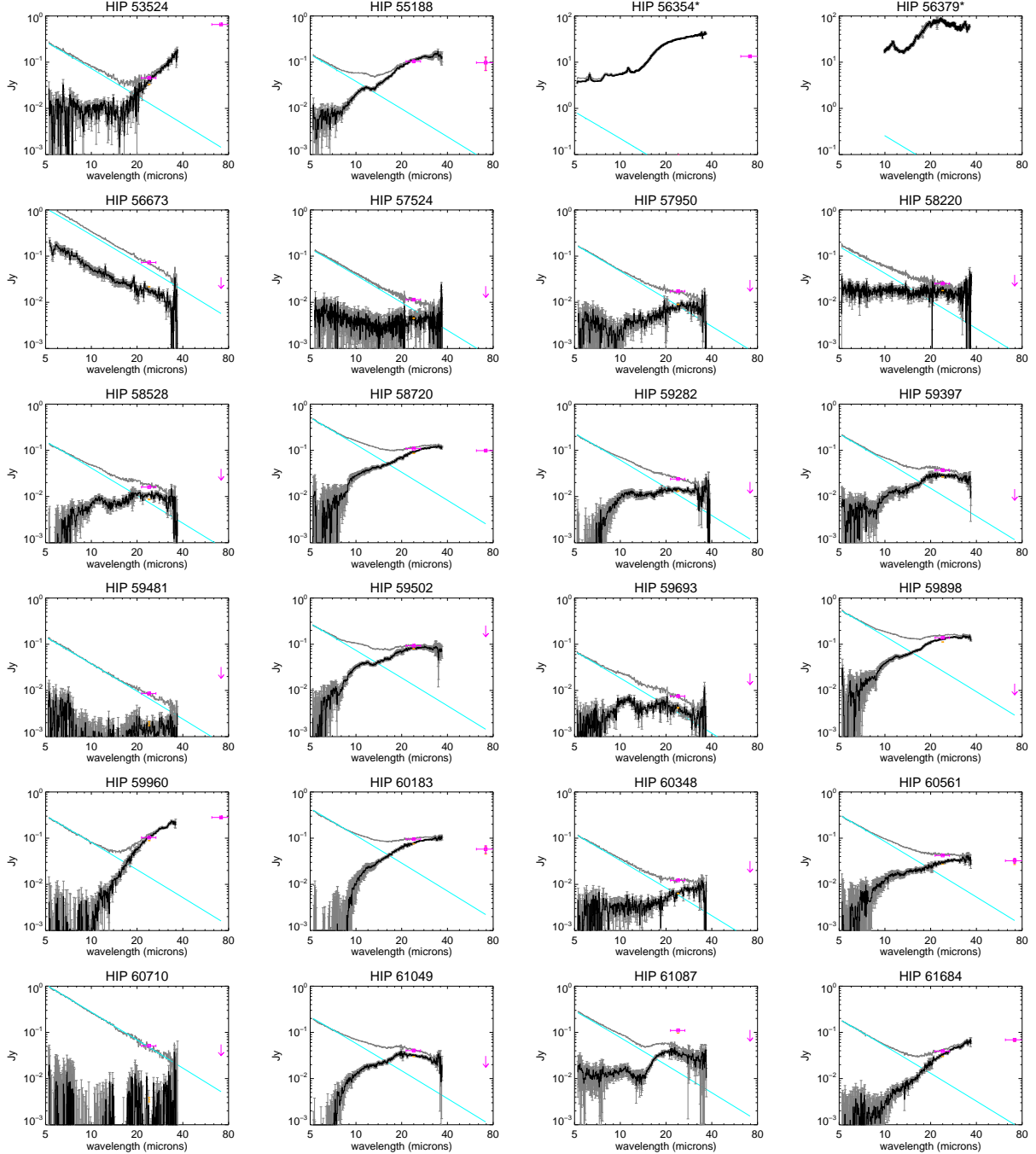


Fig. 2a.— Photosphere-subtracted spectra. The IRS spectrum is shown in gray and the photosphere fit is shown in cyan. The parameters for the photosphere fit for each star are listed in Table 1. The photosphere-subtracted spectrum is plotted in black, with gray error bars. MIPS photometric points are indicated by magenta points, with arrows indicating upper limits.

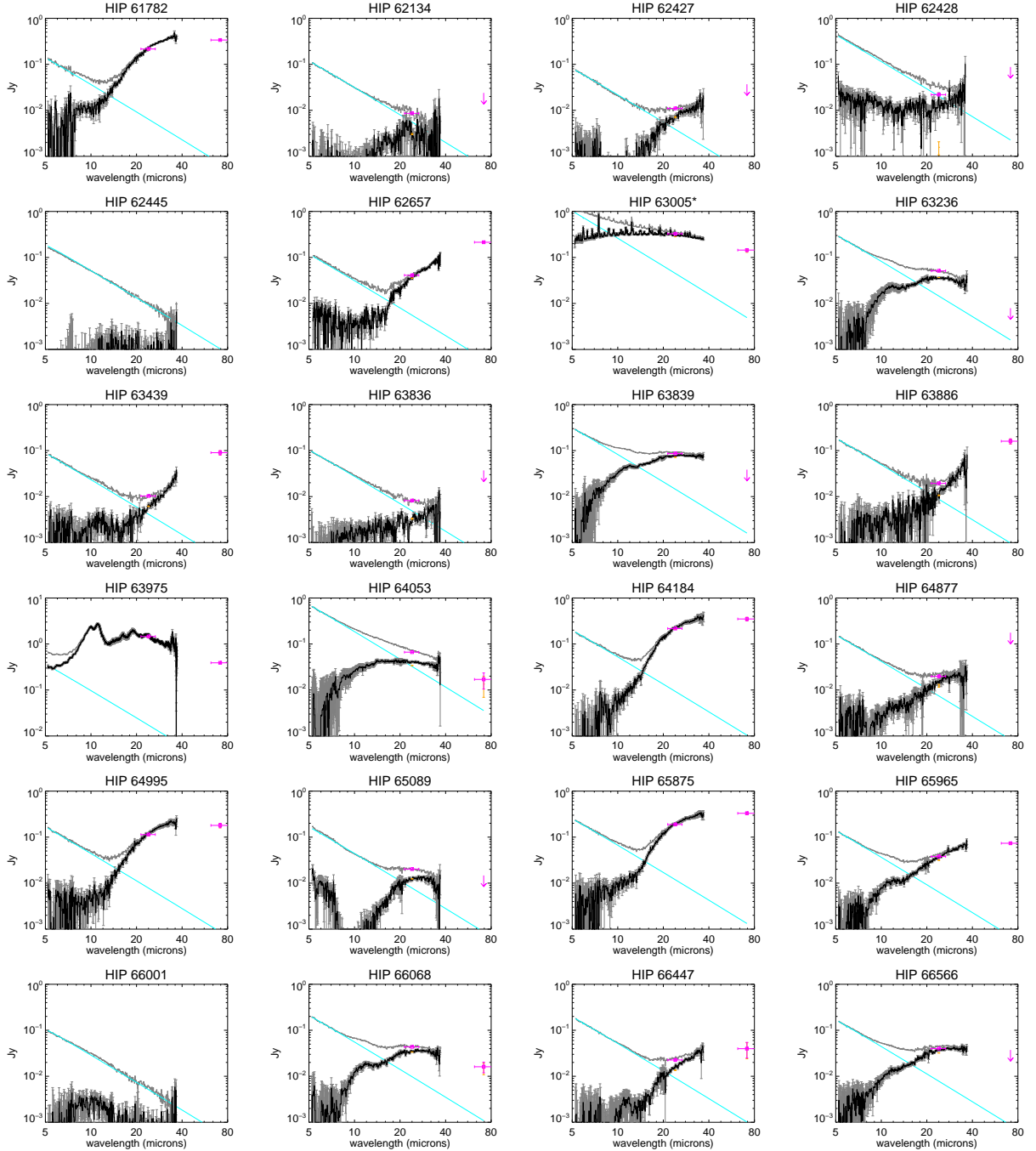


Fig. 2b.— Continuation Figure 2a, spectra of objects.

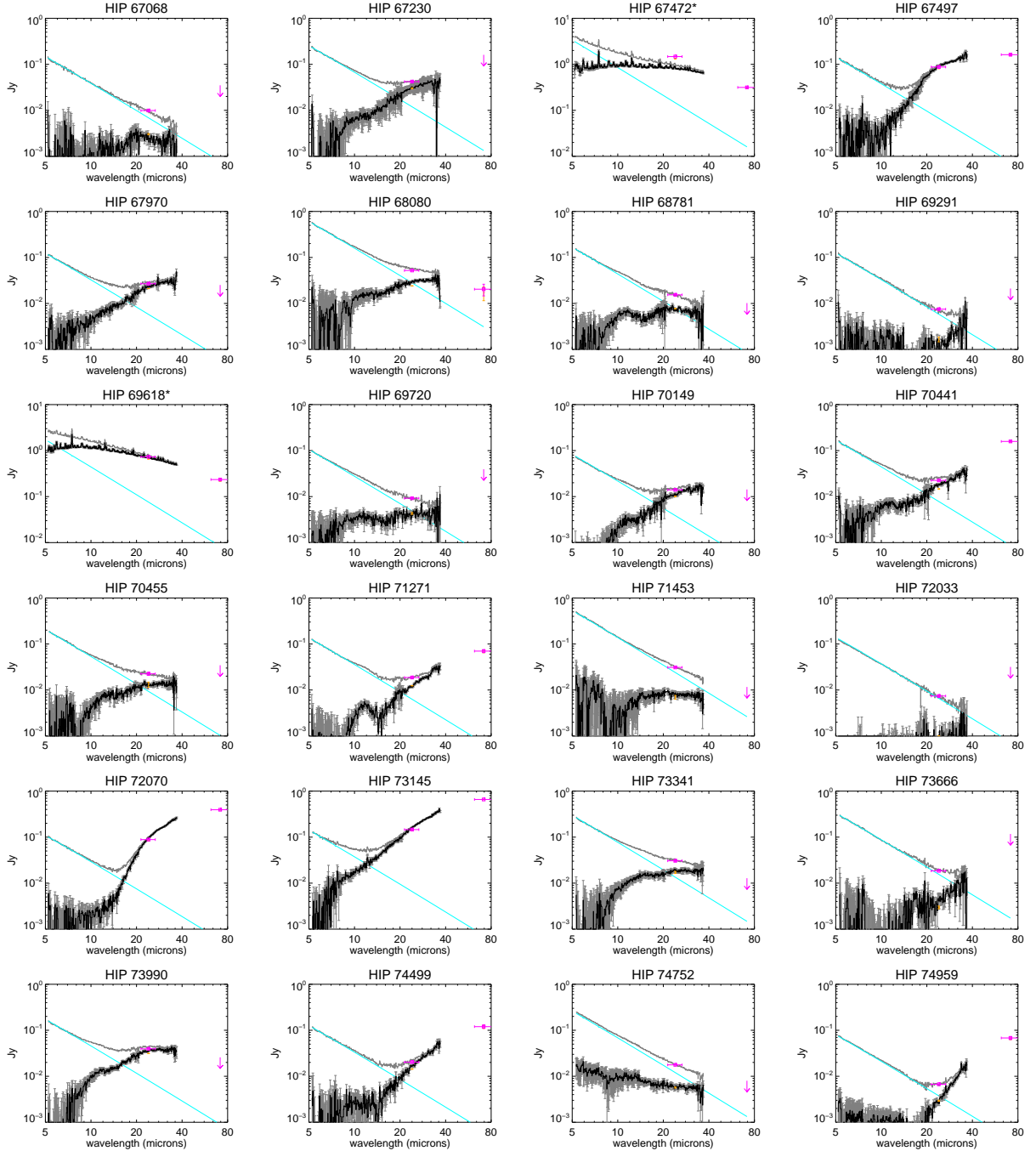


Fig. 2c.— Continuation Figure 2a, spectra of objects.

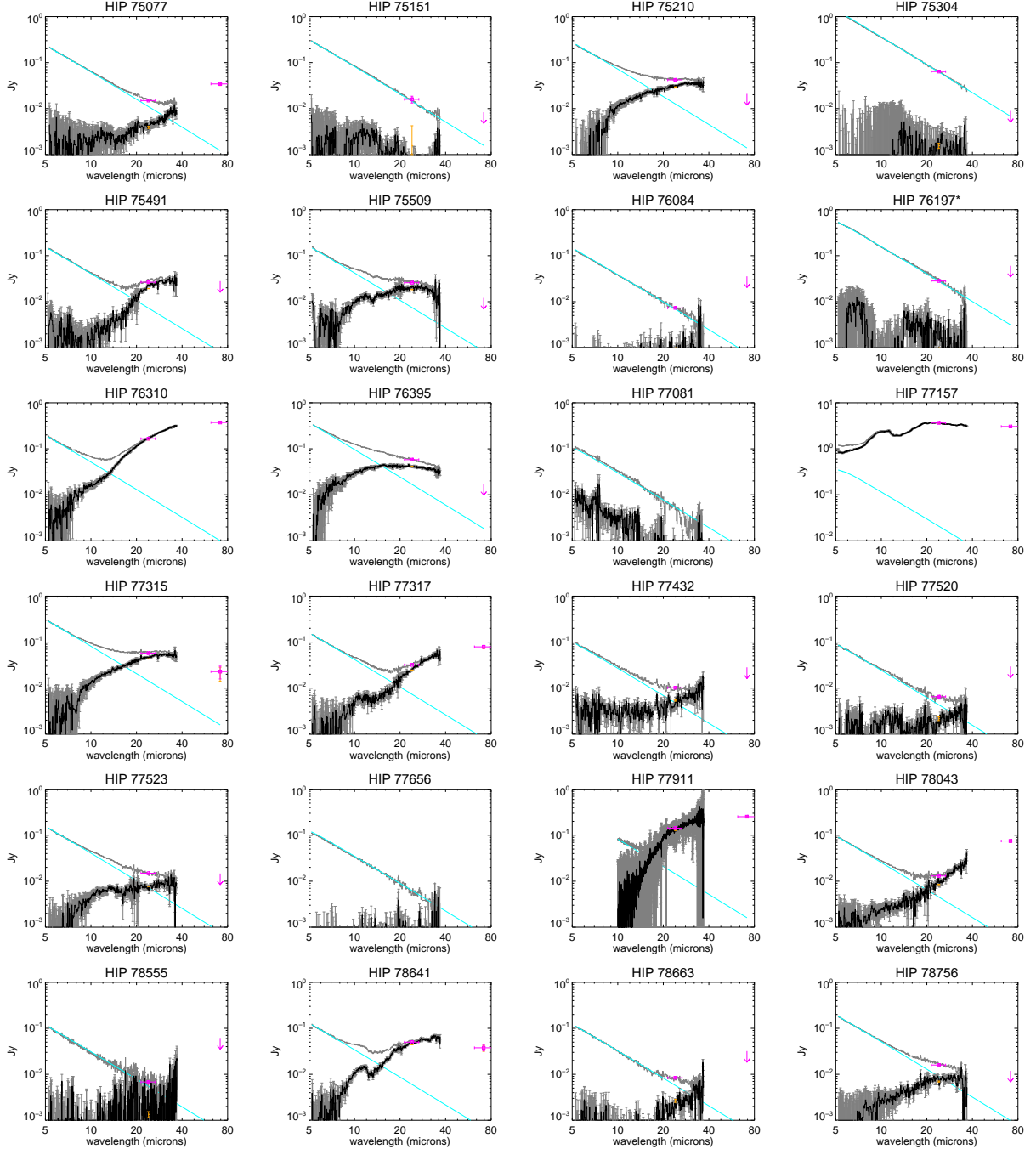


Fig. 2d.— Continuation Figure 2a, spectra of objects.

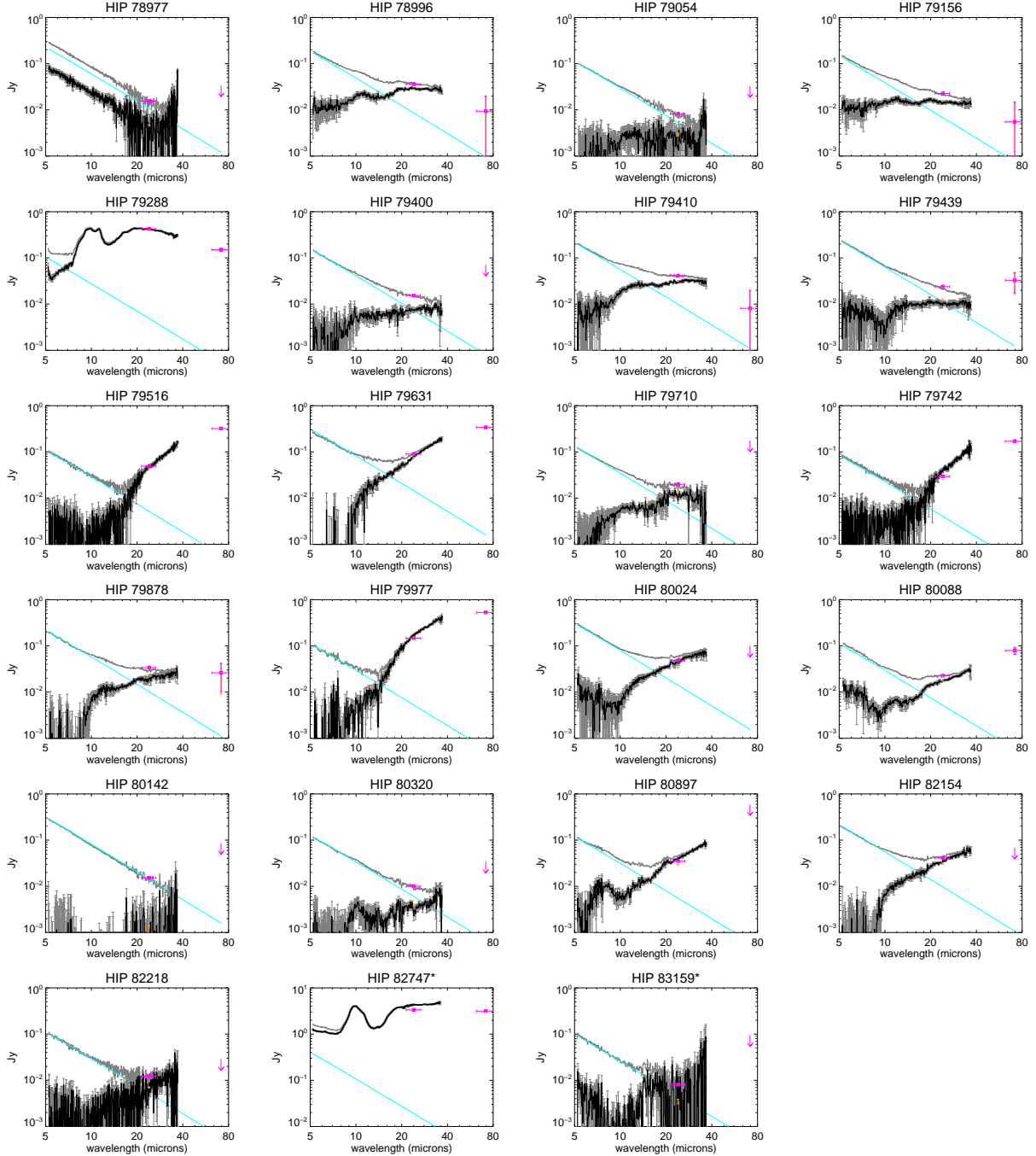


Fig. 2e.— Continuation Figure 2a, spectra of objects.

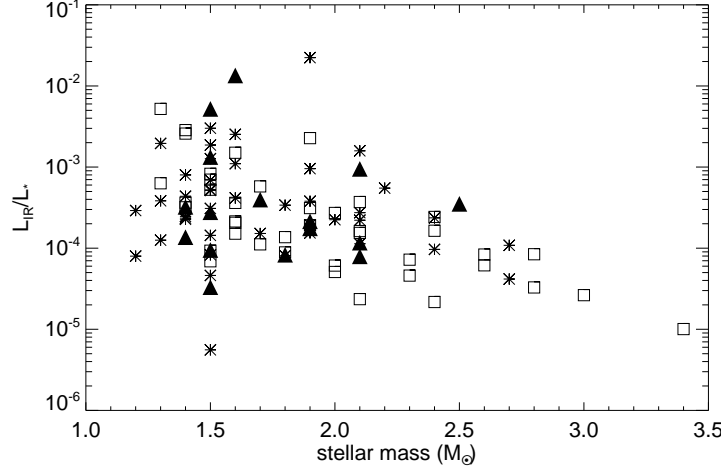


Fig. 3.— L_{IR}/L_* versus stellar mass. Asterisks are Lower Centaurus Crux, squares are Upper Centaurus Lupus, and filled triangles are Upper Scorpius.

77157 (HT Lupi), and HIP 82747 (AK Sco. See e.g. Manoj et al. 2006; Sturm et al. 2013). These sources cannot be adequately modeled using simple grain models, so we exclude them from our study. In Table 2 we tabulate the calculated L_{IR}/L_* based on the calibrated and photosphere-subtracted spectra of the remaining 110 sources. In Figure 3, we plot L_{IR}/L_* versus stellar mass. The downward trend versus stellar mass is contrary to what would be expected if disk temperatures or masses simply scale with stellar mass. This can be explained either by decreasing disk mass or decreasing dust temperature with increasing stellar mass, scenarios that will be discussed in our Results.

In general, we found that the photosphere models were consistent with the IRS observations for all of the stars in our study with the exception of HIP 56673 (HD 101088) and HIP 78977 (HD 144548). For these two objects, this normalization of the IRS spectra produced a Rayleigh-Jeans power-law excess at 5-30 μ m excess that could indicate the presence of a hot dust component with $T_{gr} \gg 500$ K. Visual spectra of HIP 56673B (HD 101088B) show time-variable H α emission, consistent with accretion observed toward T Tauri stars (Bitner et al. 2010). Alternatively, this mismatch in the MIPS 24 μ m flux and the IRS spectrum could indicate that these sources possess time variable excesses similar to that observed toward ID 8 caused by stochastic grinding events (Meng et al. 2014).

Several sources show little to no excess in the IRS data. We omit these non-excess sources based on two criteria: the excess significance and the normalized flux ratio. These quantities compare the observed versus predicted photosphere-only emission over a selected

wavelength regime. That is, if F_ν is the frequency-dependent flux with uncertainty σ_ν , then

$$F(\nu_1, \nu_2) = \frac{\int_{\nu_1}^{\nu_2} F_\nu d\nu}{\nu_2 - \nu_1} \quad (3)$$

and the weighted uncertainty is

$$\sigma^2(\nu_1, \nu_2) = \frac{\int_{\nu_1}^{\nu_2} \sigma_\nu^2 d\nu}{\nu_2 - \nu_1}. \quad (4)$$

We use the subscripts 'obs' and 'pred' to refer to the observed and predicted flux, respectively. We consider three different passbands: $8.5 - 13 \mu\text{m}$, $21 - 26 \mu\text{m}$, and $30 - 34 \mu\text{m}$. The flux integrated over each of these passbands are $F(10 \mu\text{m})$, $F(24 \mu\text{m})$, and $F(32 \mu\text{m})$, respectively.

The excess significance is defined to be

$$\chi = (F_{\text{obs}} - F_{\text{pred}}) / (\sigma_{\text{obs}}^2 + \sigma_{\text{pred}}^2)^{1/2}, \quad (5)$$

where σ_{obs} includes the repeatability error and a 5% normalization uncertainty added in quadrature, while σ_{pred} consists of a 3% normalization uncertainty. We calculate the excess significance over our three passbands, χ_{10} , χ_{24} , and χ_{32} , and list their values in Table 2. We also list values of χ_{tot} , which is the excess significance calculated over the entire IRS spectrum. HIP 56673 and HIP 78977 are listed twice: in the first listing, the IRS spectra are normalized to the MIPS 24 micron as described in Chen et al. (2014), and in the second listing, marked by an asterisk, the spectra are normalized to the photosphere model at 5-6 microns. When these sources are normalized to the photosphere, HIP 56673 exhibits a small excess, but HIP 78977 has none.

The normalized flux ratio is adapted from Carpenter et al. (2009b), and is defined to be

$$R_{32/10} = \frac{F_{\text{obs}}(32 \mu\text{m}) / F_{\text{pred}}(32 \mu\text{m})}{F_{\text{obs}}(10 \mu\text{m}) / F_{\text{pred}}(10 \mu\text{m})}. \quad (6)$$

A similar expression is used to calculate $R_{24/10}$. In Carpenter et al. (2009b), photometric fluxes were used. Here, we integrate the spectrum over the given passband, assuming 100% efficiency. Since R can be considered to be a ratio of the slope of the observed spectrum compared to the slope of the predicted spectrum, any error in the overall normalization of either spectrum cancels out. Therefore, the error on R is propagated from the repeatability error of the observed spectrum alone.

The excess significance (χ) measures the signal-to-noise of the infrared excess at each band pass, while R measures the shape of the excess. In some sources, even though the excess significance is formally low, the shape of the spectrum rises at long wavelengths, indicating

that there is a notable cold excess. If $R > 1$, then the shape of the spectrum indicates a cold excess component, while $R = 1$ indicates a shape consistent with photospheric emission. To determine which spectra to exclude as non-excess sources, we use both the χ and R measures. Sources which have χ_8 , χ_{24} , χ_{30} , and χ_{tot} all less than 3 and whose values of $R_{24/8}$ and $R_{30/8}$ are both less than or equal to 1 to within one σ are labeled non-excess sources and are excluded from further analysis. A total of 13 of our sources are non-excess sources, and are labeled as such in Table 2. In addition, HIP 78977, when normalized to the photosphere model, can be considered a non-excess source. This leaves a total of 97 debris disk spectra that we analyze for their dust properties.

Table 1. Stellar Properties

HIP	Name	Spectral Type	Distance (pc)	T_{eff} (K)	Mass (M_{\odot})	Luminosity (L_{\odot})	A_V	Program	Notes
Lower Centaurus Crux									
53524	HD 95086	A8III (6)	90.4	7499	1.6	7.11	0.000	IRS_DISKS/2	(18)
55188	HD 98363	A2V (6)	123.6	8770	1.9	11.4	0.244	CCHEN2/40235	(18)
56354	HD 100453	A9Ve (14)	121.5	7447	1.6	10.4	0.214	IRS_DISKS/2	(18) protoplanetary
56379	HD 100546	B9Vne (6)	96.9	10520	2.4	26.6	0.194	IRS_DISKS/2	(18) protoplanetary
56673	HD 101088	F5IV (6)	93.8	6440	2.2	17.7	0.142	DEBRISII/40651	(17) λ^{-2} excess
57524	HD 102458	F9IV (13)	91.7	6115	1.2	1.89	0.178	DEBRISII/40651	(17)
57950	HD 103234	F2IV/V (6)	98.1	6890	1.5	3.90	0.066	DEBRISII/40651	(17)
58220	HD 103703	F3V (6)	98.9	6740	1.5	3.35	0.096	YOUNGA/84	(17)
58528	HD 104231	F5V (6)	110.5	6440	1.4	3.73	0.016	DEBRISII/40651	(17)
58720	HD 104600	B9V (6)	105.7	11614	2.7	68.7	0.024	CCHEN2/40235	(18)
59282	HD 105613	A3V (6)	104.2	8551	1.8	11.6	0.192	CCHEN2/40235	(18)
59397	HD 105857	A2V (6)	113.0	8770	1.9	14.0	0.132	CCHEN2/40235	(18)
59481	HD 105994	F3V (7)	113.1	6740	1.5	4.09	0.023	WARMIDISK2/50538	(17)
59502	HD 106036	A2V (6)	100.7	8770	1.9	13.8	0.015	CCHEN2/40235	(18)
59693	HD 106389	F6IV (7)	137.0	6360	1.3	2.32	0.184	DEBRISII/40651	(17)
59898	HD 106797	A0V (6)	96.0	9550	2.1	32.9	0.022	CCHEN2/40235	(18)
59960	HD 106906	F5V (6)	92.1	6440	1.5	5.06	0.000	IRS_DISKS/2	(17)
60183	HD 107301	B9V (6)	93.9	10814	2.4	36.8	0.067	CCHEN2/40235	(18)
60348	HD 107649	F5V (7)	93.7	6440	1.4	2.13	0.022	YOUNGA/84	(17)
60561	HD 107947	A0V (6)	91.1	9550	2.1	17.5	0.000	CCHEN2/40235	(18)
60710	HD 108257	B3Vn (2)	137.4	17298	5.4	809.	0.070	IRS_DISKS/2	(18)
61049	HD 108857	F7V (6)	97.0	6280	1.4	3.13	0.143	CCHEN2/40235	(17)
61087	HD 108904	F6V (6)	97.5	6360	1.5	4.97	0.050	CCHEN2/40235	(17)
61684	HD 109832	A9V (6)	111.9	7447	1.6	7.14	0.261	CCHEN2/40235	(18)
61782	HD 110058	A0V (7)	107.4	9550	2.1	10.2	0.436	IRS_DISKS/2	(18)

Table 1—Continued

HIP	Name	Spectral Type	Distance (pc)	T_{eff} (K)	Mass (M_{\odot})	Luminosity (L_{\odot})	A_V	Program	Notes
62134	HD 110634	F2V (7)	115.6	6890	1.5	3.74	0.026	YOUNGA/84	(17)
62427	HD 111103	F8 (1)	142.7	6200	1.4	3.17	0.000	DEBRISII/40651	(17)
62445	HD 111170	G4.5IVe (13)	130.5	5728	1.6	4.17	0.660	RUBBLE/148	(13)
62657	HD 111520	F5/6V (7)	108.6	6400	1.3	2.60	0.028	CCHEN/241	(17)
63005	HD 112091	B5V(e) (2)	124.8	16634	5.0	541.	0.200	CCHEN2/40235	(18) classical Be
63236	HD 112383	A2IV/V (6)	110.7	8770	1.9	20.0	0.000	CCHEN2/40235	(18)
63439	HD 112810	F3/5IV/V (7)	143.3	6590	1.4	3.52	0.000	DEBRISII/40651	(17)
63836	HD 113524	F6/8 (7)	107.4	6280	1.3	2.31	0.000	DEBRISII/40651	(17)
63839	HD 113457	A0V (6)	99.4	9550	2.1	20.3	0.000	CCHEN2/40235	(18)
63886	HD 113556	F2V (6)	106.7	6890	1.5	4.91	0.024	IRS_DISKS/2	(17)
63975	HD 113766	F3/5V (7)	122.5	6590	1.9	11.9	0.000	IRS_DISKS/2	(17)
64053	HD 113902	B8/9V (7)	100.1	11695	2.7	77.6	0.070	CCHEN2/40235	(18)
64184	HD 114082	F3V (6)	85.5	6740	1.5	3.18	0.078	IRS_DISKS/2	(17)
64877	HD 115361	F5V (6)	125.0	6440	1.5	5.02	0.000	CCHEN2/40235	(17)
64995	HD 115600	F2IV/V (6)	110.5	6890	1.5	4.79	0.000	IRS_DISKS/2	(17)
65089	HD 115820	A7/8V (7)	96.5	7656	1.7	4.83	0.026	CCHEN2/40235	(18)
65875	HD 117214	F6V (6)	110.3	6360	1.6	5.64	0.000	IRS_DISKS/2	(17)
65965	HD 117484	B9.5V (7)	147.3	10593	2.4	25.9	0.100	CCHEN/40235	(18)
66001	HD 117524	G2.5IV (13)	152.4	5834	1.2	2.14	0.110	RUBBLE/148	(13)
66068	HD 117665	A1/2V (7)	147.9	8974	1.9	24.4	0.000	CCHEN/40235	(18)
66566	HD 118588	A1V (7)	126.4	9204	2.0	14.9	0.097	CCHEN/40235	(18)
67068	HD 119511	F3V (7)	91.6	6740	1.5	2.70	0.000	WARMDISK2/50538	(17)
67230	HD 119718	F5V (6)	131.8	6440	1.8	8.67	0.037	CCHEN2/40235	(17)
Upper Centaurus Lupus									
66447	HD 118379	A3IV/V (7)	121.7	8551	1.8	13.3	0.184	TD_GTO/50485	(18)
67472	HD 120324	B2V:e (8)	155.0	20512	7.3	6.53e+03	0.287	CCHEN2/40235	(18) classical Be
67497	HD 120326	F0V (7)	107.4	7200	1.6	4.45	0.158	DEBRISII/40651	(17)

Table 1—Continued

HIP	Name	Spectral Type	Distance (pc)	T_{eff} (K)	Mass (M_{\odot})	Luminosity (L_{\odot})	A_V	Program	Notes
67970	HD 121189	F3V (7)	118.8	6740	1.5	3.85	0.070	CCHEN2/40235	(17)
68080	HD 121336	A1Vn (11)	139.9	9204	2.0	64.9	0.082	CCHEN2/40235	(18)
68781	HD 122705	A4V (5)	112.9	8279	1.8	8.89	0.000	TD_GTO/50485	(18)
69291	HD 123889	F2V (9)	132.3	6890	1.5	5.02	0.043	WARMDISK2/50638	(17)
69618	HD 124367	B4Vne (2)	147.7	16982	5.2	1.01e+03	0.409	CCHEN2/40235	(18) classical Be
69720	HD 124619	F0V (6)	133.3	7200	1.6	5.00	0.228	DEBRISII/40651	(17)
70149	HD 125541	A9V (7)	113.3	7447	1.6	3.18	0.146	TD_GTO/50485	(18)
70441	HD 126062	A1V (7)	110.4	9204	2.0	11.4	0.018	CCHEN2/40235	(18)
70455	HD 126135	B8V (7)	165.0	11967	2.8	70.3	0.096	GOWERNER2005/20132	(18)
71271	HD 127750	A0V (7)	175.7	9550	2.1	26.9	0.040	TD_GTO/50485	(18)
71453	HD 128207	B8V (9)	147.5	13490	3.4	210.	0.010	GOWERNER2005/20132	(18)
72033	HD 129490	F7IV/V (7)	155.8	6280	1.5	5.46	0.297	DEBRISII/40651	(17)
72070	HD 129590	G1V (13)	132.6	5945	1.3	2.84	0.047	CCHEN2/42035	(17)
73145	HD 131835	A2IV (9)	122.7	8770	1.9	10.5	0.187	CCHEN2/40235	(18)
73341	HD 132238	B8V (9)	162.6	12359	3.0	112.	0.040	GOWERNER2005/20132	(18)
73666	HD 133075	F3IV (9)	151.5	6740	2.1	16.5	0.364	DEBRISII/40651	(17)
73990	HD 133803	A9V (9)	124.8	7447	1.6	8.04	0.211	TD_GTO/50485	(18)
74499	HD 134888	F3/5V (9)	89.9	6590	1.5	2.06	0.058	DEBRISII/40651	(17)
74752	HD 135454	B9.5V (7)	173.3	10351	2.3	66.2	0.023	GOWERNER2005/20132	(18)
74959	HD 135953	F5V (9)	133.2	6440	1.3	2.68	0.080	TD_GTO/50485	(17)
75077	HD 136246	A1V (9)	131.6	9204	2.0	22.7	0.114	GOWERNER2005/20132	(18)
75151	HD 136347	B9IVSi(SrCr) (11)	143.3	11641	2.7	68.2	0.031	GOWERNER2005/20132	(18)
75210	HD 136482	B8/9V (9)	136.2	11324	2.6	54.2	0.033	GOWERNER2005/20132	(18)
75304	HD 136664	B4V (2)	159.2	16711	5.0	1.27e+03	0.052	IREXT/20294	(18)
75491	HD 137057	F3V (9)	168.6	6740	1.9	9.59	0.051	CCHEN2/40235	(17)
75509	HD 137119	A2V (9)	107.2	8770	1.9	9.02	0.067	CCHEN2/40235	(18)
76084	HD 138296	F2V (9)	142.7	6890	1.7	6.64	0.191	DEBRISII/40651	(17)
76395	HD 138923	B8V (3)	106.5	11967	2.8	53.6	0.041	GOWERNER2005/20132	(18)
77081	HD 140374	G7.5IV (13)	200.8	5521	1.4	2.24	0.150	RUBBLE/148	(13)

Table 1—Continued

HIP	Name	Spectral Type	Distance (pc)	T_{eff} (K)	Mass (M_{\odot})	Luminosity (L_{\odot})	A_V	Program	Notes
77157	HT Lupi	K3Ve (15)	141.2	4730	1.1	5.09	1.138	CCHEN2/40235	(17) protoplanetary
77315	HD 140817	A0V (9)	147.3	9550	2.1	41.5	0.105	CCHEN2/40235	(18)
77317	HD 140840	B9/A0V (9)	125.8	10593	2.4	21.5	0.029	CCHEN2/40235	(18)
77432	HD 141011	F5V (7)	96.3	6440	1.4	1.90	0.000	DEBRISII/40651	(17)
77520	HD 141254	F3V (9)	100.8	6740	1.5	1.87	0.194	WARM DISK2/50538	(17)
77523	HD 141327	B9V (9)	195.3	10304	2.3	48.3	0.139	TD_GTO/50485	(18)
77656	HD 141521	G5IV (13)	140.1	5702	1.4	2.57	0.520	RUBBLE/148	(13)
78043	HD 142446	F3V (9)	144.3	6740	1.5	4.66	0.124	TD_GTO/50485	(17)
78555	HD 143538	F0V (9)	106.3	7200	1.6	3.55	0.178	CCHEN/241	(17)
78641	HD 143675	A5IV/V (9)	113.4	8072	1.7	6.32	0.049	CCHEN2/40235	(18)
78756	HD 143939	B9III (10)	144.7	10740	2.4	40.6	0.000	TD_GTO/50485	(18)
79400	HD 145357	A5V (7)	146.8	8072	1.7	12.8	0.342	TD_GTO/50485	(18)
79516	HD 145560	F5V (7)	133.7	6440	1.4	3.84	0.001	CCHEN/241	(17)
79631	HD 145880	B9.5V (9)	127.9	10593	2.4	35.3	0.355	TD_GTO/50485	(18)
79710	HD 145972	F0V (7)	127.4	7200	1.6	5.78	0.094	TD_GTO/50485	(17)
79742	HD 146181	F6V (19)	146.2	6360	1.4	3.66	0.000	CCHEN/241	(17)
80142	HD 147001	B7V (7)	137.2	11912	2.8	78.5	0.166	TD_GTO/50485	(18)
80897	HD 148657	A0V (9)	165.6	9550	2.1	21.3	0.864	TD_GTO/50485	(18)
82154	HD 151109	B8V (4)	222.7	11298	2.6	117.	0.074	TD_GTO/50485	(18)
82747	AK Sco	F5V (9)	102.8	6440	1.5	4.72	1.098	IRSDISKS/2	(17) protoplanetary
83159	HD 153232	F5V (9)	146.6	6440	1.5	4.17	0.000	CCHEN/241	(17)

Upper Scorpius

76310	HD 138813	A0V (16)	150.8	9750	2.1	30.5	0.155	JMCARP/30091	(20)
77859	HD 142184	B2V (12)	130.9	JMCARP/30091	classical Be
77911	HD 142315	B9V (19)	147.7	10000	2.5	50.2	0.202	JMCARP/30091	(20)
78207	HD 142983	B8Ia/Iab (12)	143.5	JMCARP/30091	classical Be
78663	HD 143811	F5V (9)	144.3	6440	1.5	4.86	0.093	DEBRISII/40651	(17)

Table 1—Continued

HIP	Name	Spectral Type	Distance (pc)	T_{eff} (K)	Mass (M_{\odot})	Luminosity (L_{\odot})	A_V	Program	Notes
78977	HD 144548	F7V (15)	116.7	6280	1.5	5.02	0.365	CCHEN/241	(17) λ^{-2} excess
78996	HD 144587	A9V (16)	108.5	8750	1.4	11.4	0.967	JMCARP/30091	(20)
79054	HD 144729	F0V (12)	138.9	7200	1.5	5.47	0.585	CCHEN/241	(17)
79156	HD 144981	A0V (16)	170.4	9750	1.9	31.6	0.574	JMCARP/30091	(20)
79288	HD 145263	F0V (12)	149.9	7200	1.6	6.40	0.399	DEBRISII/40651	(17)
79410	HD 145554	B9V (16)	140.4	10000	1.9	32.5	0.577	JMCARP/30091	(20)
79439	HD 145631	B9V (16)	131.8	10000	1.8	32.7	0.666	JMCARP/30091	(20)
79878	HD 146606	A0V (16)	129.4	10000	2.1	27.1	0.016	JMCARP/30091	(20)
79977	HD 146897	F2/3V (12)	122.7	6815	1.5	3.66	0.341	IRS_DISKS/2	(17)
80024	HD 147010	B9II (16)	163.4	10500	2.1	73.7	0.772	JMCARP/30091	(20)
80088	HD 147137	A9V (19)	139.1	9000	1.7	12.7	1.147	JMCARP/30091	(20)
80320	HD 147594	G3IV (15)	142.0	5830	1.4	3.39	0.031	WARMDISK2/50538	(17)
82218	HD 151376	F2/3V (12)	135.7	6815	1.5	4.48	0.300	CCHEN/241	(17)

References. — References: (1) Cannon & Pickering (1920), (2) Hiltner et al. (1969), (3) Hube (1970), (4) Schild et al. (1971), (5) Glaspey (1972), (6) Houk & Cowley (1975), (7) Houk (1978), (8) Morgan et al. (1978), (9) Houk (1982), (10) Gahm et al. (1983), (11) Corbally (1984), (12) Houk & Smith-Moore (1988), (13) Mamajek et al. (2002), (14) Vieira et al. (2003), (15) Torres et al. (2006), (16) Preibisch & Mamajek (2008), (17) Chen et al. (2011), (18) Chen et al. (2012), (19) Pecaut et al. (2012), (20) Chen et al. (2014)

Table 2. Inferred disk properties

HIP	HD name	L_{IR}/L_{\ast}	excess significance (χ)				$R_{24/10}$	$R_{32/10}$	a_{min} (μm)	note
			χ_{10}	χ_{24}	χ_{32}	total				
Lower Centaurus Crux										
53524	HD 95086	1.10e-03	1.85	7.10	9.75	2.13	3.21 ± 0.30	12.53 ± 1.08	1.8	
55188	HD 98363	9.56e-04	6.47	16.55	7.98	5.19	9.97 ± 0.31	23.44 ± 2.65	2.3	
56673	HD 101088	5.50e-04	2.86	4.37	2.90	2.91	1.12 ± 0.02	1.11 ± 0.07	3.2	λ^{-2} excess
56673*	HD 101088	4.42e-05	0.23	2.00	1.30	0.28	1.12 ± 0.02	1.11 ± 0.07	3.2	*
57524	HD 102458	2.91e-04	1.27	2.56	2.13	1.19	1.40 ± 0.19	1.79 ± 0.41	0.4	
57950	HD 103234	1.44e-04	0.96	7.04	4.65	0.97	1.76 ± 0.07	2.45 ± 0.30	1.1	
58220	HD 103703	6.91e-04	4.40	6.30	4.24	3.50	2.19 ± 0.23	3.17 ± 0.60	0.9	
58528	HD 104231	2.35e-04	2.47	7.48	3.55	1.15	1.98 ± 0.12	2.57 ± 0.47	1.1	
58720	HD 104600	1.09e-04	3.25	15.10	17.02	2.44	3.72 ± 0.06	8.04 ± 0.16	8.6	
59282	HD 105613	8.07e-05	2.40	9.26	4.78	0.94	1.91 ± 0.06	2.58 ± 0.33	2.5	
59397	HD 105857	1.74e-04	2.32	12.06	9.20	1.95	3.01 ± 0.13	4.39 ± 0.34	2.8	
59481	HD 105994	8.28e-05	0.17	1.86	1.16	0.42	1.19 ± 0.09	1.39 ± 0.34	1.1	
59502	HD 106036	3.79e-04	5.49	13.80	5.17	3.38	4.71 ± 0.18	8.45 ± 1.45	2.8	
59693	HD 106389	3.83e-04	3.48	4.58	2.27	1.57	1.67 ± 0.18	1.87 ± 0.47	0.7	
59898	HD 106797	2.21e-04	3.85	16.05	17.48	3.11	4.31 ± 0.06	8.23 ± 0.14	5.5	
59960	HD 106906	1.27e-03	0.44	13.60	16.09	2.49	7.11 ± 0.35	23.54 ± 1.04	1.4	
60183	HD 107301	9.65e-05	1.60	15.08	14.85	1.74	4.06 ± 0.14	8.46 ± 0.40	5.4	
60348	HD 107649	2.27e-04	1.50	6.69	3.92	1.07	1.83 ± 0.11	3.03 ± 0.51	0.4	
60561	HD 107947	1.13e-04	2.33	11.31	10.33	1.49	2.44 ± 0.08	4.33 ± 0.27	3.1	
60710	HD 108257	-2.13e-06	-0.43	-0.11	0.25	-0.21	1.02 ± 0.07	1.11 ± 0.31	44.7	no excess
61049	HD 108857	4.36e-04	3.46	12.94	10.42	1.86	3.13 ± 0.09	4.16 ± 0.25	0.9	
61087	HD 108904	5.24e-04	2.43	5.69	1.95	1.88	2.93 ± 0.35	3.58 ± 1.38	1.4	
61684	HD 109832	4.16e-04	1.14	13.01	15.03	1.79	3.93 ± 0.13	10.36 ± 0.39	1.8	
61782	HD 110058	1.58e-03	3.69	17.41	18.00	6.63	23.13 ± 1.24	72.52 ± 3.83	1.9	
62134	HD 110634	4.61e-05	0.08	1.59	0.27	0.15	1.59 ± 0.36	1.34 ± 1.24	1.0	
62427	HD 111103	2.46e-04	-0.57	7.19	5.17	0.57	2.76 ± 0.22	6.38 ± 1.02	0.9	
62445	HD 111170	-1.57e-04	-0.12	0.31	-0.01	-0.58	1.04 ± 0.10	1.01 ± 0.39	1.1	no excess
62657	HD 111520	1.96e-03	1.81	14.82	17.50	3.49	5.97 ± 0.23	20.37 ± 0.70	0.8	
63236	HD 112383	1.54e-04	2.57	12.60	10.61	1.73	2.71 ± 0.12	3.76 ± 0.26	3.9	
63439	HD 112810	8.00e-04	1.38	6.25	10.92	1.18	2.00 ± 0.16	6.48 ± 0.47	1.0	
63836	HD 113524	1.26e-04	1.00	4.34	2.42	0.47	1.46 ± 0.09	2.56 ± 0.66	0.7	
63839	HD 113457	2.74e-04	5.07	15.37	16.07	3.34	4.13 ± 0.14	7.12 ± 0.26	3.6	

Table 2—Continued

HIP	HD name	L_{IR}/L_{\ast}	excess significance (χ)				$R_{24/10}$	$R_{32/10}$	a_{min} (μm)	note
			χ_{10}	χ_{24}	χ_{32}	total				
63886	HD 113556	5.15e-04	0.84	4.68	4.88	0.75	2.05 ± 0.22	6.74 ± 1.15	1.3	
63975	HD 113766	2.23e-02	17.40	18.78	14.00	13.12	4.00 ± 0.11	4.93 ± 0.27	2.5	
64053	HD 113902	4.17e-05	2.27	9.93	8.92	1.28	1.89 ± 0.04	2.54 ± 0.14	9.6	
64184	HD 114082	3.01e-03	1.83	13.19	9.41	3.82	19.43 ± 1.17	56.92 ± 5.46	0.8	
64877	HD 115361	3.09e-04	1.22	5.85	1.86	1.04	2.59 ± 0.25	5.43 ± 2.41	1.4	
64995	HD 115600	1.87e-03	1.57	12.22	8.98	3.49	12.76 ± 0.88	40.36 ± 4.16	1.3	
65089	HD 115820	1.52e-04	-0.32	9.60	6.66	1.21	2.46 ± 0.09	3.65 ± 0.36	1.2	
65875	HD 117214	2.53e-03	2.14	13.25	9.56	4.05	13.32 ± 0.72	37.70 ± 3.41	1.5	
65965	HD 117484	2.37e-04	3.10	14.72	14.76	2.92	4.93 ± 0.18	13.81 ± 0.64	3.9	
66001	HD 117524	7.98e-05	1.31	0.88	-0.01	0.28	1.04 ± 0.13	0.91 ± 0.42	0.6	no excess
66068	HD 117665	1.94e-04	3.18	13.91	11.39	2.17	3.45 ± 0.10	5.71 ± 0.34	4.6	
66566	HD 118588	2.24e-04	3.00	14.26	11.26	2.69	4.32 ± 0.16	8.16 ± 0.55	2.9	
67068	HD 119511	5.58e-06	0.28	3.79	2.30	0.03	1.33 ± 0.07	1.52 ± 0.23	0.7	
67230	HD 119718	3.39e-04	1.51	4.08	3.30	1.05	2.99 ± 0.49	6.06 ± 1.56	2.0	
Upper Centaurus Lupus										
66447	HD 118379	1.37e-04	0.45	10.08	10.05	0.80	2.44 ± 0.10	6.29 ± 0.46	2.8	
67497	HD 120326	1.50e-03	1.31	15.53	15.65	3.50	11.52 ± 0.70	31.39 ± 2.00	1.1	
67970	HD 121189	5.25e-04	2.13	11.04	12.42	2.10	3.93 ± 0.23	8.62 ± 0.52	1.0	
68080	HD 121336	6.10e-05	1.27	8.88	9.60	0.83	1.81 ± 0.04	2.83 ± 0.14	10.9	
68781	HD 122705	8.87e-05	1.93	7.62	4.35	0.96	1.72 ± 0.06	2.18 ± 0.27	2.0	
69291	HD 123889	6.89e-05	0.62	2.22	2.62	0.38	1.14 ± 0.06	1.71 ± 0.28	1.4	
69720	HD 124619	1.51e-04	1.97	5.28	3.49	0.98	1.59 ± 0.11	2.18 ± 0.36	1.3	
70149	HD 125541	2.06e-04	1.57	9.20	7.94	1.22	3.28 ± 0.21	6.80 ± 0.68	0.8	
70441	HD 126062	2.72e-04	1.99	9.09	9.59	1.57	2.68 ± 0.15	6.52 ± 0.51	2.2	
70455	HD 126135	3.28e-05	1.35	7.62	6.47	1.01	2.08 ± 0.12	3.25 ± 0.33	8.5	
71271	HD 127750	1.62e-04	1.32	10.74	12.09	1.10	2.51 ± 0.08	7.01 ± 0.37	4.6	
71453	HD 128207	1.01e-05	0.34	4.17	5.05	0.52	1.29 ± 0.04	1.53 ± 0.08	19.5	
72033	HD 129490	-1.06e-04	-0.20	0.45	0.64	-0.48	1.06 ± 0.09	1.23 ± 0.34	1.5	no excess
72070	HD 129590	5.22e-03	1.15	18.03	18.66	5.45	15.21 ± 0.43	60.57 ± 1.80	0.9	
73145	HD 131835	2.27e-03	5.10	17.74	17.89	6.89	14.32 ± 0.69	49.81 ± 2.48	2.2	
73341	HD 132238	2.64e-05	1.63	7.60	6.90	0.93	2.03 ± 0.11	3.06 ± 0.28	12.2	
73666	HD 133075	2.36e-05	-0.13	2.35	2.85	0.13	1.25 ± 0.08	1.99 ± 0.33	3.1	
73990	HD 133803	3.62e-04	2.95	14.05	12.14	2.30	4.12 ± 0.16	7.35 ± 0.44	2.0	
74499	HD 134888	8.25e-04	1.10	8.84	12.42	1.27	3.14 ± 0.22	10.34 ± 0.67	0.3	

Table 2—Continued

HIP	HD name	L_{IR}/L_{\ast}	excess significance (χ)				$R_{24/10}$	$R_{32/10}$	a_{min} (μm)	note
			χ_{10}	χ_{24}	χ_{32}	total				
74752	HD 135454	7.22e-05	1.70	4.89	5.94	1.61	1.29 ± 0.08	1.61 ± 0.11	9.7	
74959	HD 135953	6.31e-04	0.80	4.85	10.84	0.85	1.60 ± 0.11	5.59 ± 0.35	0.8	
75077	HD 136246	5.09e-05	0.57	3.55	6.70	0.41	1.31 ± 0.07	2.07 ± 0.13	4.1	
75151	HD 136347	5.01e-06	0.49	0.58	0.21	0.18	1.01 ± 0.04	0.99 ± 0.10	8.5	no excess
75210	HD 136482	6.14e-05	2.53	11.56	10.42	1.62	2.78 ± 0.10	5.03 ± 0.32	7.1	
75304	HD 136664	-3.90e-06	-0.26	0.32	0.21	-0.42	1.04 ± 0.04	1.04 ± 0.05	73.8	no excess
75491	HD 137057	3.12e-04	0.67	11.41	10.90	1.35	3.45 ± 0.16	7.43 ± 0.51	2.0	
75509	HD 137119	1.92e-04	3.38	9.02	4.78	2.13	2.77 ± 0.17	4.03 ± 0.64	1.9	
76084	HD 138296	-7.25e-05	-0.31	0.50	0.10	-0.44	1.07 ± 0.09	1.06 ± 0.35	1.6	no excess
76395	HD 138923	8.42e-05	4.39	12.14	12.72	2.77	2.48 ± 0.07	3.61 ± 0.14	6.6	
77081	HD 140374	3.63e-04	1.36	-0.52	-0.45	0.96	0.85 ± 0.11	0.68 ± 0.47	0.1	no excess
77315	HD 140817	1.54e-04	2.69	12.88	13.92	2.15	3.39 ± 0.11	6.34 ± 0.26	6.9	
77317	HD 140840	1.64e-04	1.82	10.72	14.39	1.79	3.63 ± 0.19	10.90 ± 0.48	3.3	
77432	HD 141011	3.19e-04	1.65	3.85	3.14	1.30	1.74 ± 0.21	3.26 ± 0.76	0.2	
77520	HD 141254	9.31e-05	1.18	2.47	2.58	0.47	1.28 ± 0.13	2.07 ± 0.43	0.2	
77523	HD 141327	4.59e-05	1.86	6.65	4.79	0.92	1.77 ± 0.10	2.87 ± 0.39	7.2	
77656	HD 141521	-1.73e-04	-0.41	-0.06	-0.03	-0.61	1.02 ± 0.15	1.00 ± 0.33	0.7	no excess
78043	HD 142446	7.00e-04	1.60	5.90	9.73	1.46	2.54 ± 0.25	7.80 ± 0.60	1.3	
78555	HD 143538	-7.40e-05	-0.52	0.52	0.34	-0.21	1.29 ± 0.47	1.55 ± 1.51	0.9	no excess
78641	HD 143675	5.77e-04	4.11	15.67	14.25	3.61	6.15 ± 0.18	14.16 ± 0.66	1.5	
78756	HD 143939	2.17e-05	0.82	5.42	4.14	0.52	1.73 ± 0.11	2.53 ± 0.36	5.9	
79400	HD 145357	1.11e-04	1.47	5.35	8.60	0.95	1.75 ± 0.16	2.63 ± 0.20	2.9	
79516	HD 145560	2.85e-03	0.59	14.18	15.53	2.82	8.20 ± 0.56	33.35 ± 2.30	1.1	
79631	HD 145880	2.43e-04	1.20	15.19	17.19	1.73	5.18 ± 0.26	17.28 ± 0.88	5.2	
79710	HD 145972	2.14e-04	2.39	7.07	3.32	1.26	2.42 ± 0.19	3.27 ± 0.72	1.5	
79742	HD 146181	2.59e-03	1.24	8.71	14.00	2.62	8.12 ± 0.98	32.95 ± 3.14	1.1	
80142	HD 147001	-1.42e-05	-0.92	-0.03	0.20	-0.47	1.06 ± 0.27	1.19 ± 0.54	9.4	no excess
80897	HD 148657	3.71e-04	3.05	15.32	16.48	3.81	5.96 ± 0.25	17.90 ± 0.79	3.7	
82154	HD 151109	8.35e-05	1.94	13.05	12.35	1.75	3.73 ± 0.12	9.06 ± 0.51	14.6	
83159	HD 153232	5.23e-04	0.32	0.46	0.34	0.39	1.81 ± 1.80	3.91 ± 9.26	1.1	no excess
Upper Scorpius										
76310	HD 138813	9.50e-04	4.36	18.00	17.65	6.55	12.95 ± 0.39	39.23 ± 1.38	5.2	
77911	HD 142315	3.52e-04	0.11	2.58	1.75	0.75	8.83 ± 4.33	25.22 ± 16.45	7.0	
78663	HD 143811	3.30e-05	-0.15	2.48	2.20	0.06	1.34 ± 0.12	2.18 ± 0.53	1.3	

Table 2—Continued

HIP	HD name	L_{IR}/L_{\ast}	excess significance (χ)				$R_{24/10}$	$R_{32/10}$	a_{min} (μm)	note
			χ_{10}	χ_{24}	χ_{32}	total				
78977	HD 144548	1.33e-03	4.72	1.60	1.38	4.52	0.97 ± 0.15	1.50 ± 0.53	1.4	λ^{-2} excess
78977*	HD 144548	9.55e-05	0.21	-0.13	0.90	0.10	0.97 ± 0.15	1.50 ± 0.53	1.4	no excess*
78996	HD 144587	3.24e-04	4.70	13.91	11.09	3.37	2.93 ± 0.10	4.80 ± 0.31	3.1	
79054	HD 144729	9.49e-05	1.15	1.09	0.55	0.51	1.33 ± 0.37	1.50 ± 1.07	1.5	no excess
79156	HD 144981	2.15e-04	4.66	10.36	8.08	3.09	2.16 ± 0.10	3.27 ± 0.28	5.9	
79288	HD 145263	1.35e-02	18.25	19.36	19.13	16.29	5.84 ± 0.08	8.87 ± 0.15	1.6	
79410	HD 145554	1.76e-04	4.38	12.65	10.87	2.68	2.86 ± 0.11	4.95 ± 0.32	6.0	
79439	HD 145631	8.33e-05	1.16	6.31	5.77	1.20	1.72 ± 0.11	2.47 ± 0.26	6.4	
79878	HD 146606	7.98e-05	1.72	6.34	5.92	1.01	2.47 ± 0.22	4.50 ± 0.59	4.6	
79977	HD 146897	5.21e-03	1.71	15.88	15.25	4.94	24.15 ± 1.87	89.38 ± 7.21	1.0	
80024	HD 147010	1.17e-04	1.70	7.70	7.76	2.12	3.54 ± 0.30	8.22 ± 0.86	11.6	
80088	HD 147137	3.98e-04	2.41	11.77	14.09	2.90	3.44 ± 0.16	7.91 ± 0.36	2.9	
80320	HD 147594	1.37e-04	1.09	4.65	3.22	0.45	1.44 ± 0.09	2.22 ± 0.38	1.0	
82218	HD 151376	2.77e-04	0.52	3.21	2.78	0.55	2.07 ± 0.35	4.75 ± 1.39	1.2	

*HIP 56673 and HIP 78977 are listed twice, the marked listing indicating that the spectrum was normalized to the photosphere model rather than the MIPS 24 micron measurement.

3. Debris Disk Modeling

Our modeling of the dust in the debris disks under study goes beyond a simple blackbody model. This is because the spectral range covered by IRS includes various silicate features. In order to model the IRS spectra in better detail, we include grain properties such as size, temperature, and composition and generate model spectra using Mie theory.

3.1. Optical Properties of Grains

We assume that the dust is composed of amorphous silicates of olivine and pyroxene composition, the optical constants for which are adopted from Dorschner et al. (1995) and Jaeger et al. (1994), assuming a Mg : Fe ratio of 1 for both species³.

In order to calculate equilibrium temperatures, we need the optical constants at short wavelengths as well. For $\lambda \lesssim 2\mu\text{m}$, we use the optical constants for astronomical silicates from Draine & Lee (1984).

The minimum grain size, a_{\min} , is estimated by assuming that radiation pressure removes the smallest grains if $\beta (= F_{\text{rad}}/F_{\text{grav}}) > 0.5$, so that

$$a_{\min} > \frac{6L_* \langle Q_{\text{pr}}(a) \rangle}{16\pi G M_* c \rho_s} \quad (7)$$

(Artymowicz 1988), where L_* and M_* are the stellar luminosity and mass, ρ_s is the density of an individual grain, and $\langle Q_{\text{pr}}(a) \rangle$ is the spectrum-averaged radiation pressure coupling coefficient, given by $\langle Q_{\text{pr}}(a) \rangle = \int Q_{\text{pr}}(a, \lambda) F_\lambda d\lambda / (\int F_\lambda d\lambda)$. These values are tabulated in Chen et al. (2011) for F- and G-type stars, and Chen et al. (2012) for B- and A-type stars. In Table 1 we list the stellar mass and luminosity assumed for modeling the dust for each source, and in Table 2, we list the estimated minimum grain size.

Chen et al. (2011, 2012) estimated the color temperature of the dust from the the ratio of 24 to 70 micron MIPS photometric excess, and the grain distance calculated assuming the grains had a temperature equal to the color temperature and a size equal to an average grain size of $\langle a \rangle = 5a_{\min}/3$. The IRS spectra provide more detailed information on the temperature, size, and composition of the dust grains than the MIPS photometry. In this work we allow the grain size to be a free parameter. The distribution of grain sizes depends

³ Optical constants for all silicate species are available at <http://www.astro.uni-jena.de/Laboratory/OCDB/newsilicates.html>.

on the model type implemented, as described in §3.3, and a_{\min} is treated as a lower limit on grain size.

For computational simplicity, we use Mie theory to calculate the optical constants for scattering and absorption of light on particles of different sizes. The main element missing from a Mie-theory treatment would be grain porosity, which could result in underestimating the grain sizes and β values (Lisse et al. 1998; Kolokolova et al. 2007, 2001). We use the Oxford IDL routines⁴ to calculate the optical constants. This generates $Q^{\text{ext}}(\lambda, a)$ and $Q^{\text{sca}}(\lambda, a)$, the extinction and scattering efficiencies, respectively, as a function of wavelength λ and grain radius a . Then the absorption efficiency is $Q^{\text{abs}} = Q^{\text{ext}} - Q^{\text{sca}}$. Scattered stellar light does not contribute significantly at the Spitzer IRS wavelengths, so we consider only the thermal component of emission in modeling the spectra.

3.2. Grain Temperatures and Distances

The dust grains are assumed to be heated by stellar irradiation and in thermal equilibrium. The amount of radiation absorbed by a grain is the incident stellar flux modified by the absorption efficiency Q_{abs} scaled by the cross-section of the grain. The absorption efficiencies of olivine and pyroxene are Q_o^{abs} and Q_p^{abs} , respectively. The fractional composition of olivine is f_o , so the fractional composition of pyroxene is $(1 - f_o)$. The stellar flux at a distance r from the star is $F_{\nu,*} = \pi(R_*/r)^2 I_{\nu,*}(T_{\text{eff}})$. Then the total power absorbed by a grain is

$$P_{\text{abs}} = \int_0^{\infty} \pi^2 a^2 Q^{\text{abs}} \left(\frac{R_*}{r} \right)^2 I_{\nu,*}(T_{\text{eff}}) d\nu \quad (8)$$

where $I_{\nu,*}$ is the stellar spectrum, for which we use the best fit Kurucz models.

The total emergent power of a grain of radius a and temperature T_{gr} is

$$P_{\text{emit}} = \int_0^{\infty} 4\pi^2 a^2 Q^{\text{abs}} B_{\nu}(T_{\text{gr}}) d\nu \quad (9)$$

where B_{ν} is the Planck function.

To find the equilibrium temperature of the grain, we set $P_{\text{emit}} = P_{\text{abs}}$ and find that

$$\int_0^{\infty} Q^{\text{abs}} B_{\nu}(T_{\text{gr}}) d\nu = \frac{R_*^2}{4r^2} \int_0^{\infty} Q^{\text{abs}} I_{\nu,*}(T_{\text{eff}}) d\nu \quad (10)$$

⁴ <http://www-atm.physics.ox.ac.uk/code/mie/index.html>

The absorption efficiency, Q_{abs} , is itself a function of a and ν , and also depends on the composition, as determined from Mie theory and the optical constants of the constituents, namely oliving and pyroxene. We set Q^{abs} equal to the the absorption efficiencies of olivine (Q_o^{abs}) or pyroxene (Q_p^{abs}), depending on the grain composition. We assume a segregated spheres distribution for the composition of grains where each grain is either pure olivine or pure pyroxene, and f_o and f_p are the mass fraction of grains consisting of olivine or pyroxene, respectively. The distance of the grains derived from the grain temperatures is sensitive to the composition. For instance, highly reflective grains, such as ices, absorb energy less efficiently, therefore for the same equilibrium temperature they will be at smaller stellocentric distances compared to more absorptive grains. For olivine and pyroxene, we find that the differences in distances are not significant. We also find that including a wider range of compositions, such as crystalline silicates, does not significantly improve fits to the mid-IR spectra enough to justify the additional free parameters. Thus, the scope of this work is limited to olivine and pyroxene compositions only.

To facilitate calculations of equilibrium temperatures, we tabulate values of r versus T_{gr} as a function of a and composition and interpolate on the grid. The equilibrium temperature of a grain of a given size is a proxy for its distance from the star.

We assume that the disks are optically thin, so the total spectrum of the disk is the summation of the emission of all the grains in the disk. We define $n(a, r)$ to be the number density of grains between distance r and $r + \delta r$ and grain size a and $a + \delta a$ grain size distribution as a function of a and r so that the total number of grains is $N = \int \int n(a, r) 2\pi r dr da$ and the total mass of the disk is

$$M = \int \int \frac{4\pi a^3}{3} \rho_d n(a, r) 2\pi r dr da \quad (11)$$

where ρ_d is the bulk density of the dust grains (3.3 g/cm^3). The emitted spectrum of a single grain of radius a at a distance r from the star is

$$\pi \frac{a^2}{d^2} Q_{\text{abs}}(a, \lambda) B_\nu[T_{\text{gr}}(T_{\text{eff}}, a, r)]$$

where d is the distance between the observer and the star. Thus, the total integrated spectrum for a distribution of particles in a disk is

$$F_\nu = \int \int \pi \frac{a^2}{d^2} Q_{\text{abs}}(a, \lambda) B_\nu[T_{\text{gr}}(T_{\text{eff}}, a, r)] n(a, r) 2\pi r dr da. \quad (12)$$

3.3. Fitting the Spectra

We fit our spectra to two different dust distribution models, allowing grain size, temperature/distance, and composition to be free parameters in order to understand the properties of the debris disks. The model types were 1) a single uniform grain size with a single temperature and composition, and 2) a two grain model where each population has a uniform grain size, temperature, and composition. In each case, the best fitting size and temperature parameters are determined by minimizing the reduced χ^2_ν . This was implemented using the IDL routine MPFITFUN. The detailed description of each model follows, including a listing of the free parameters for each model type.

1. *Single grain model:* This model assumes a population of grains of a uniform single size and temperature, as if they were distributed in a ring (or a shell) of uniform radius around the star. The free parameters for this model are the grain radius a , temperature T_{gr} , and composition (f_o, f_p) . The total number of particles N sets the overall normalization of the spectrum. Since the grain size distribution and stellocentric distance are delta functions, then the brightness of this model disk assuming a distance of d is

$$F_\nu = N \frac{\pi a^2}{d^2} [f_o Q_o^{\text{abs}}(a, \lambda) + f_p Q_p^{\text{abs}}(a, \lambda)] B_\nu(T_{\text{gr}}). \quad (13)$$

This mass of this disk is then

$$M_{\text{disk}} = N \frac{4\pi a^3}{3} \rho_d. \quad (14)$$

Our assumption is that all the grains are at the same temperature. If the absorption efficiencies were to differ greatly between olivine and pyroxene, then the grains would not be co-located at the same distance from the star. For the grain sizes and temperature ranges explored, the absorption efficiencies are similar enough that the dust grains are effectively co-located. For typical temperatures and grain sizes in our fits, the calculated distances between pure olivine and pure pyroxene grains differs by $\sim 10\%$.

2. *Two-grain model:*

This model is a superposition of two uniform grain populations, each with its own independent grain size, temperature, and composition. That is, one ring of grains with grain radius a_1 , temperature T_1 , composition (f_{o1}, f_{p1}) , and number N_1 , plus a second ring with parameters a_2 , T_2 , (f_{o2}, f_{p2}) , and N_2 . Then the brightness of this disk model is

$$F_\nu = N_1 \frac{\pi a_1^2}{d_1^2} [f_{o1} Q_o^{\text{abs}}(a_1, \nu) + f_{p1} Q_p^{\text{abs}}(a_1, \nu)] (a_1, \nu) B_\nu(T_1)$$

$$+ N_2 \frac{\pi a_2^2}{d_2^2} [f_{o,2} Q_o^{\text{abs}}(a_2, \nu) + f_{p,2} Q_p^{\text{abs}}(a_2, \nu)] B_\nu(T_2). \quad (15)$$

This mass of this disk is then

$$M_{\text{disk}} = \left(N_1 \frac{4\pi a_1^3}{3} + N_2 \frac{4\pi a_2^3}{3} \right) \rho_d \quad (16)$$

4. Results

For each fit, the grain temperature, grain size, and amorphous silicate composition are allowed to be free parameters. That is, the single grain model has 4 free parameters (temperature, grain size, olivine:pyroxene ratio, and total mass), and the two-grain model has 8 free parameters. Once we have carried out a least-squares fit to the excess spectrum of the single-grain and two-grain population models, as described in section 3.3, we need to determine which model best describes each object. If the reduced χ_ν^2 value is less than 2, then we declare the fit to be reasonable. The resulting fits for the 96 sources analyzed are shown in Tables 3-5. These tables also list the derived stellocentric distance of each grain population, r_{gr} , which is calculated from the fitted grain properties and assumed stellar properties, according to Equation (10). In Figures 4a-4e, we show these fits to the infrared excess spectra. In each plot, the photosphere-subtracted spectrum is plotted, along with the best fit single-grain and two-grain models to the excess spectrum.

If the single grain model is a reasonable fit for a given object, then that object is considered a single-belt debris system. If the single grain model is not a reasonable fit for the object but the two-grain model is, then we consider that object a two-belt debris system. Upon visual inspection, we found 10 objects whose formal χ_ν^2 values for a single grain model are less than 2, but have much better fits to the two-grain model, and are best explained by noisiness of the spectra. We re-categorize these objects as two-belt systems. Similarly, 5 objects have formal χ_ν^2 greater than 2 for a single grain model, but are not significantly better fit by a two grain model, and we re-classify these as single belt systems. An additional 11 systems have χ_ν^2 for both fits larger than 2, but are mostly well-fit by a two grain model, and we re-categorize them as two belt systems. Most of the objects in the latter two groups have mismatches at the short wavelength part of the spectrum, which is most affected by the normalization of the stellar photosphere. HIP 55188 (Figure 4a) is one of the systems for which neither model produces a good fit, although it is clear that the two-grain model produces a much better fit than the single-grain model for this particular case. For each fit, the grain temperature, grain size, and amorphous silicate composition are allowed to be free parameters. (Note: HIP 55188 is well-fit if we include crystalline silicates.) In total, we have 48 objects that are single-belt systems and 44 that are two-belt systems.

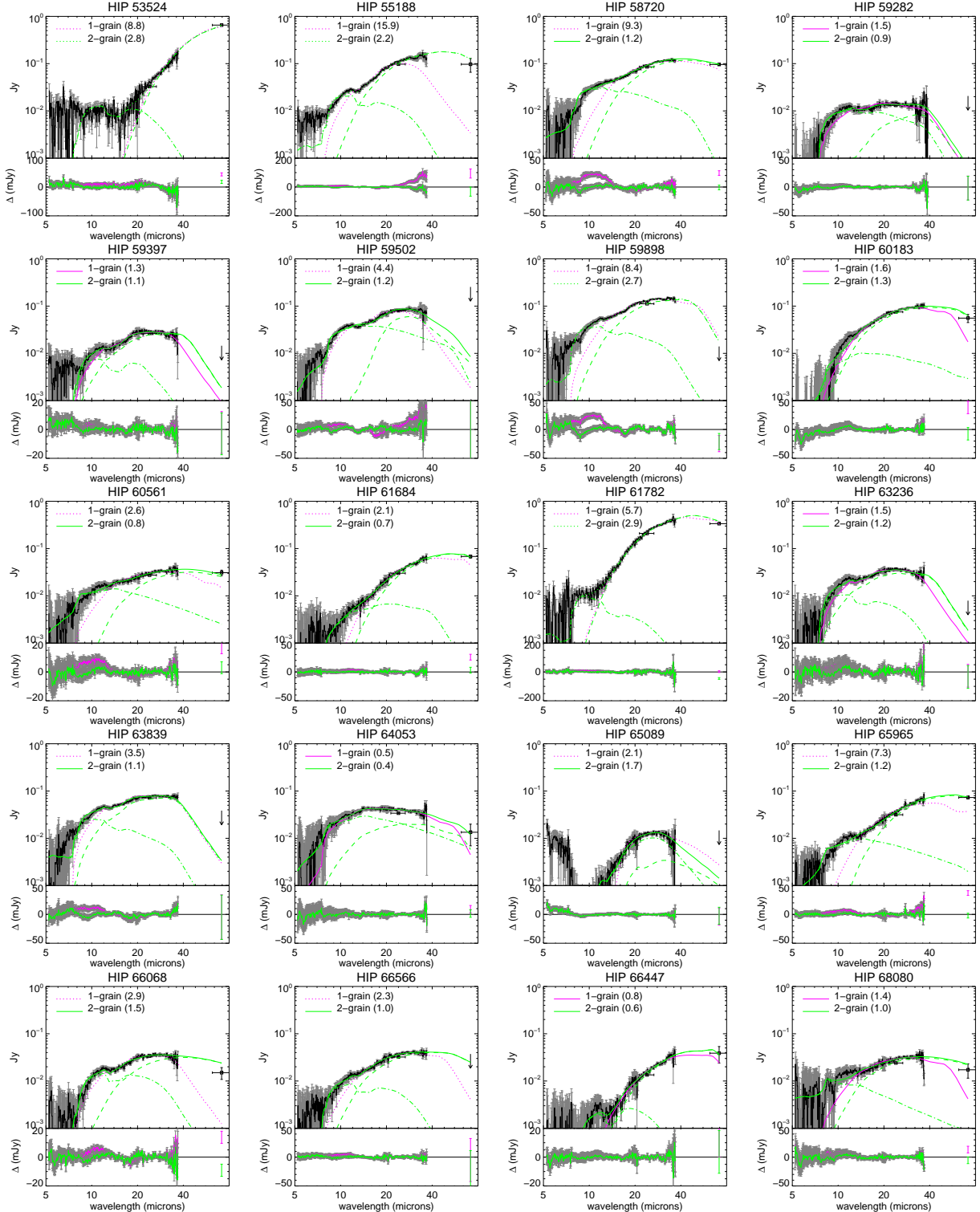


Fig. 4a.— Best fit single grain and two-grain models to photosphere-subtracted infrared spectra. Solid lines indicate a good ($\chi^2_\nu < 2$) fit, while dotted lines indicated a poor fit. The single grain fit is plotted in magenta, and the two-grain fit is plotted in green, with the two components plotted as dashed and dot-dashed lines. The lower panel of each plot shows the residuals after the fit.

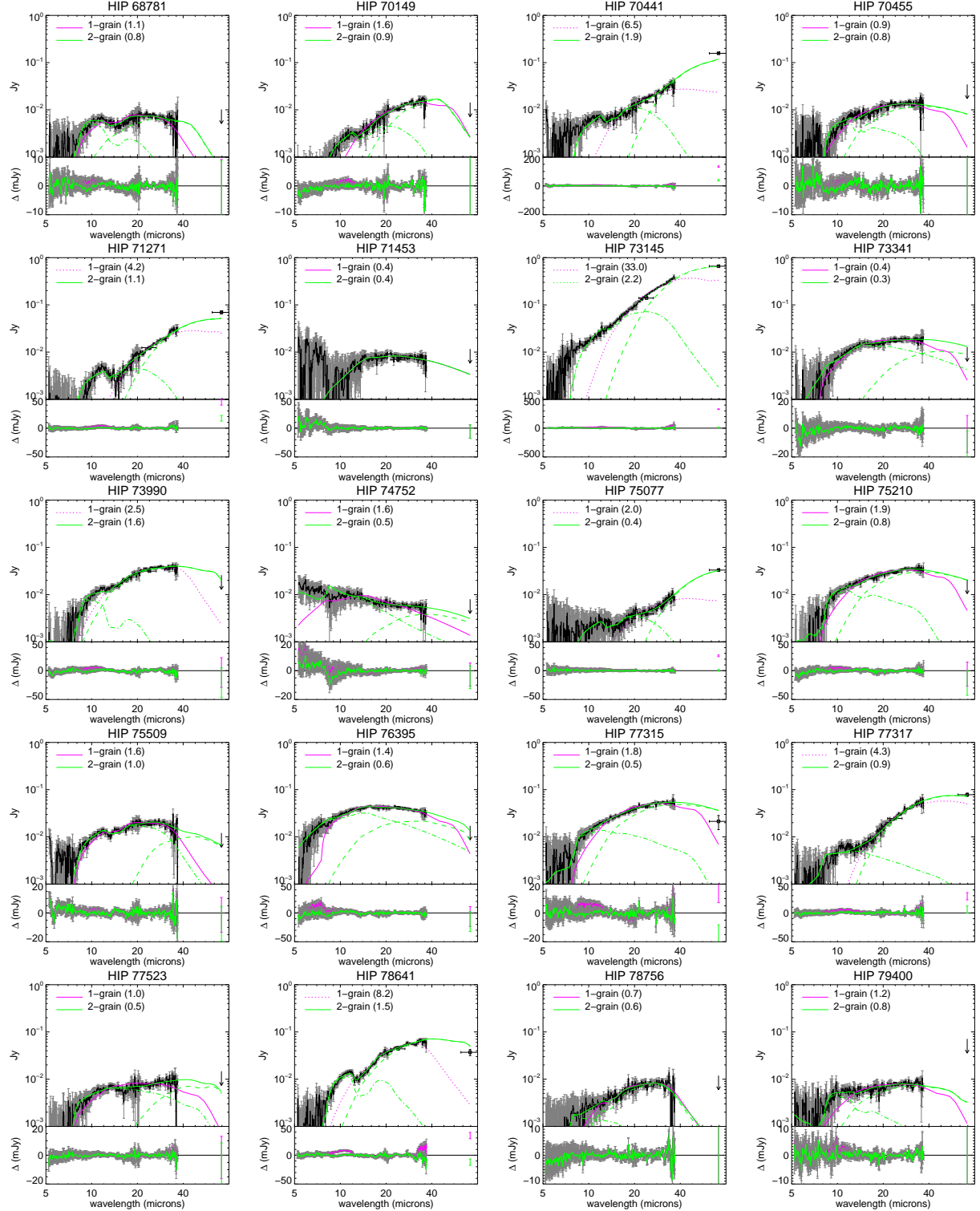


Fig. 4b.— Continuation Figure 4a.

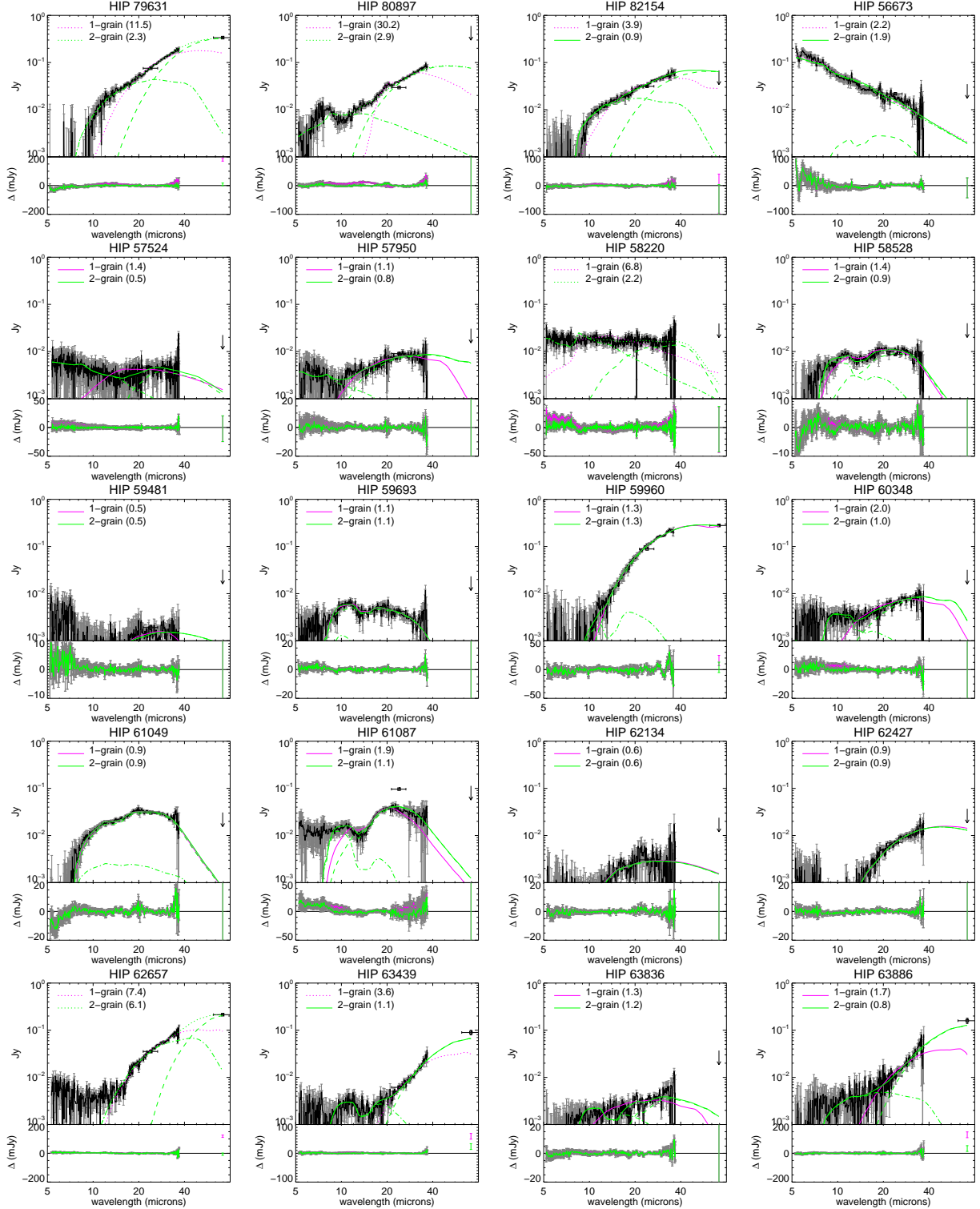


Fig. 4c.— Continuation Figure 4a.

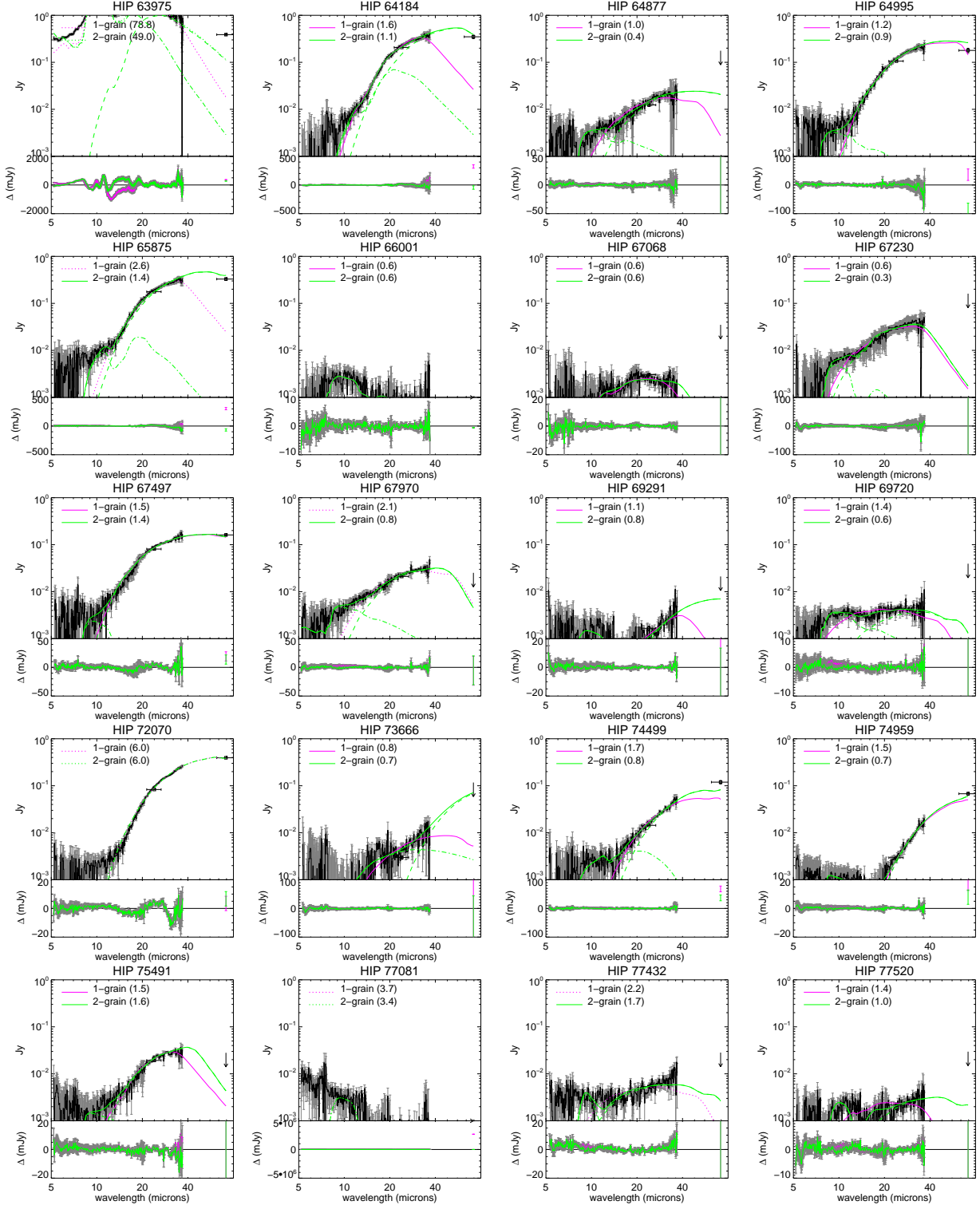


Fig. 4d.— Continuation Figure 4a.

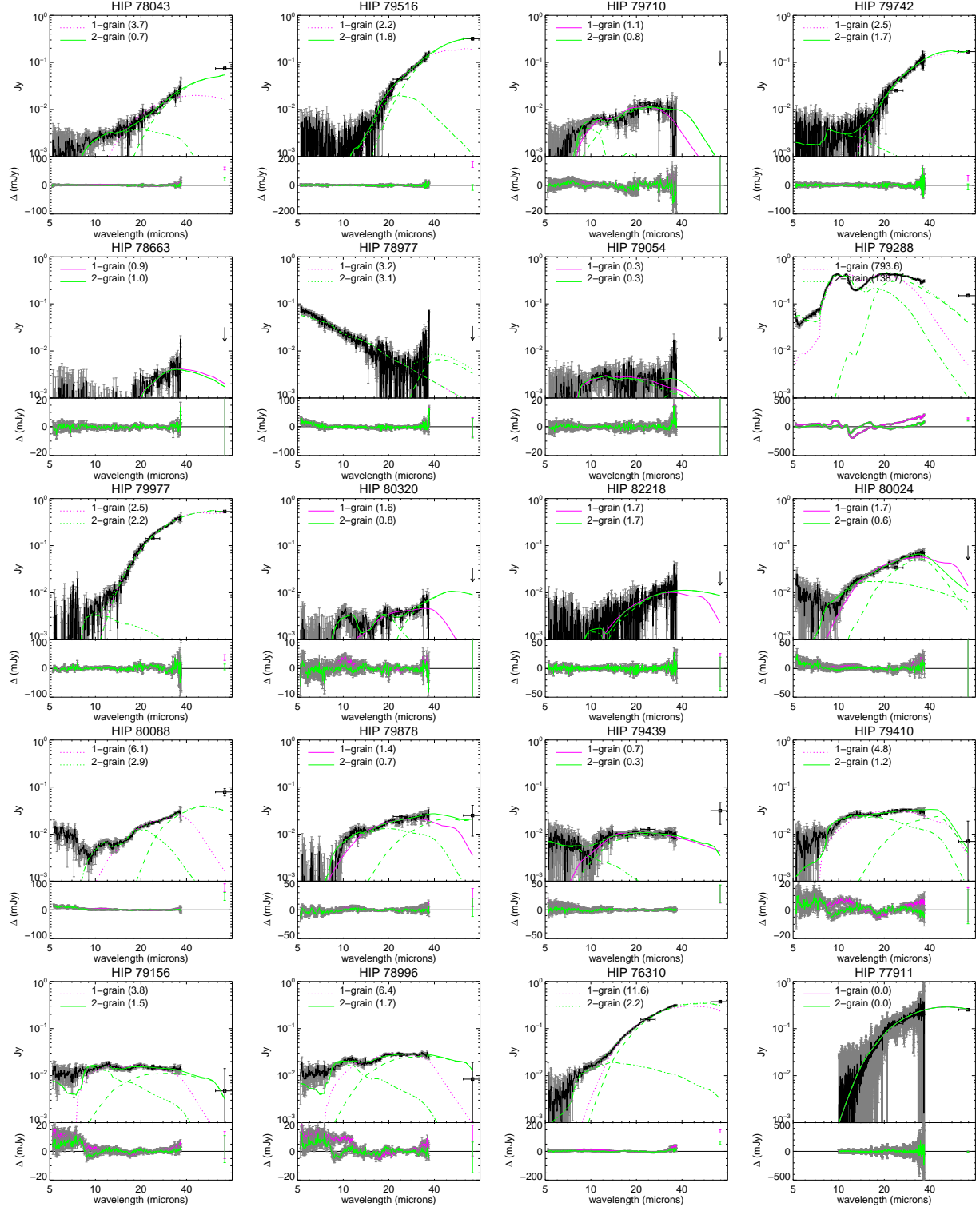


Fig. 4e.— Continuation Figure 4a.

Table 3. Fits to single grain model

HIP ID	χ^2_ν	T_{gr} (K)	a_{gr} (μm)	mass (M_{moon})	f_o	r_{gr} (AU)
#HIP 56673	0.93	267 \pm 12	7.59 \pm 0.83	1.75e-05	0.00 \pm 0.00	3.69 \pm 0.33
*HIP 56673	2.19	1480 \pm 40	198 \pm 8	9.38e-05	0.00 \pm 0.00	0.151 \pm 0.02
HIP 57524	1.41	246 \pm 4	85 \pm 4.3	2.12e-04	0.00 \pm 0.00	1.73 \pm 0.12
HIP 57950	1.14	203 \pm 2	8.07 \pm 0.25	4.39e-05	0.00 \pm 0.00	2.93 \pm 0.36
HIP 58528	1.39	274 \pm 1	4.68 \pm 0.08	1.77e-05	0.00 \pm 0.00	1.63 \pm 0.17
HIP 59282	1.50	274 \pm 2	6.37 \pm 0.12	2.94e-05	0.00 \pm 0.00	2.92 \pm 0.26
HIP 59397	1.27	216 \pm 1	5.24 \pm 0.05	1.07e-04	0.00 \pm 0.00	5.15 \pm 0.43
HIP 59481	0.47	176 \pm 4	4.98 \pm 0.42	1.03e-05	0.00 \pm 0.00	4.1 \pm 0.55
HIP 59693	1.11	438 \pm 4	4.28 \pm 0.1	3.41e-06	0.54 \pm 0.11	0.618 \pm 0.07
HIP 59960	1.29	108 \pm 0.3	11.2 \pm 0.1	1.20e-02	1.00 \pm 0.00	12.3 \pm 3.4
HIP 60348	1.95	182 \pm 2	8.87 \pm 0.23	5.64e-05	0.00 \pm 0.00	2.65 \pm 0.13
HIP 61049	0.92	250 \pm 0.5	4.9 \pm 0.03	5.47e-05	0.00 \pm 0.00	1.74 \pm 0.5
HIP 61087	1.85	208 \pm 1	3.27 \pm 0.07	7.75e-05	0.13 \pm 0.11	3.49 \pm 0.38
HIP 62134	0.60	175 \pm 6	1030 \pm 160	1.02e-02	1.00 \pm 0.00	5.3 \pm 1
HIP 62427	0.91	112 \pm 1	37.2 \pm 2	7.02e-03	1.00 \pm 0.00	10 \pm 1.4
HIP 63236	1.53	235 \pm 1	5.22 \pm 0.03	1.00e-04	0.00 \pm 0.00	5.2 \pm 0.61
HIP 63836	1.26	227 \pm 4	8.92 \pm 0.36	1.79e-05	0.00 \pm 0.00	1.81 \pm 0.3
HIP 64053	0.50	294 \pm 1	9.52 \pm 0.1	1.08e-04	0.00 \pm 0.00	6.61 \pm 0.87
HIP 64877	1.00	167 \pm 2	8.85 \pm 0.35	2.94e-04	0.00 \pm 0.00	4.83 \pm 0.48
HIP 64995	1.24	114 \pm 1	9.48 \pm 0.29	1.14e-02	0.97 \pm 0.28	10.7 \pm 1.4
*HIP 65089	2.13	93.1 \pm 0.7	0.102 \pm 0.01	1.70e-03	0.59 \pm 0.07	131 \pm 15
HIP 66447	0.83	114 \pm 1	10 \pm 0.3	2.04e-03	0.84 \pm 0.22	17.7 \pm 2
HIP 67068	0.63	226 \pm 8	4.48 \pm 0.44	4.62e-06	0.25 \pm 0.70	2.07 \pm 0.36
HIP 67497	1.53	124 \pm 0.4	15.5 \pm 0.2	9.96e-03	1.00 \pm 0.00	8.82 \pm 1
HIP 68781	1.06	276 \pm 2	4.9 \pm 0.08	1.36e-05	0.00 \pm 0.00	2.56 \pm 0.35
HIP 69291	1.09	102 \pm 2	5.89 \pm 0.43	1.71e-04	1.00 \pm 0.00	15.3 \pm 1.7
HIP 69720	1.36	285 \pm 4	7.92 \pm 0.27	1.63e-05	0.00 \pm 0.00	1.77 \pm 0.26
HIP 70455	0.94	216 \pm 2	8.93 \pm 0.19	1.95e-04	0.00 \pm 0.00	11.5 \pm 1.3
HIP 71453	0.43	224 \pm 6	119 \pm 12	2.18e-03	0.80 \pm 0.71	21.1 \pm 4.1
*HIP 72070	5.98	93.7 \pm 0.1	16.2 \pm 0.1	7.98e-02	1.00 \pm 0.00	12.2 \pm 2.3
HIP 73341	0.44	242 \pm 2	9.57 \pm 0.19	2.09e-04	0.00 \pm 0.00	11.9 \pm 1.6
HIP 73666	0.83	132 \pm 4	14.8 \pm 1.5	7.65e-04	0.00 \pm 0.00	14.5 \pm 1.5
HIP 74752	1.63	401 \pm 7	138 \pm 5	6.23e-04	0.00 \pm 0.00	4.1 \pm 0.45
HIP 74959	1.52	68.6 \pm 0.6	15.9 \pm 0.8	2.38e-02	1.00 \pm 0.00	21.8 \pm 2.2
HIP 75491	1.52	125 \pm 0.2	5.12 \pm 0.05	1.41e-03	0.00 \pm 0.00	13.5 \pm 1.3
HIP 75509	1.58	251 \pm 1	5.13 \pm 0.07	4.37e-05	0.00 \pm 0.00	3.09 \pm 0.5

Table 3—Continued

HIP ID	χ^2_ν	T_{gr} (K)	a_{gr} (μm)	mass (M_{moon})	f_o	r_{gr} (AU)
HIP 76395	1.39	306 \pm 1	9.53 \pm 0.07	1.13e-04	0.00 \pm 0.00	5.32 \pm 0.73
*HIP 77432	2.17	228 \pm 3	8.75 \pm 0.4	2.19e-05	0.00 \pm 0.00	1.62 \pm 0.63
HIP 77520	1.36	243 \pm 4	5.63 \pm 0.26	5.68e-06	0.00 \pm 0.00	1.44 \pm 0.19
HIP 77523	1.02	268 \pm 3	8.96 \pm 0.22	9.43e-05	0.00 \pm 0.00	6.56 \pm 1
HIP 77911	0.04	112 \pm 1	29.4 \pm 1	1.02e-01	1.00 \pm 0.00	38.5 \pm 5.6
HIP 78663	0.95	67 \pm 0.9	2.23 \pm 0.41	6.40e-03	0.00 \pm 0.00	91.8 \pm 9.1
HIP 78756	0.68	204 \pm 1	5.26 \pm 0.13	5.96e-05	0.00 \pm 0.00	9.55 \pm 1
*HIP 78977	3.18	1500 \pm 0	2690 \pm 10	8.00e-04	0.00 \pm 0.00	0.0781 \pm 0.01
HIP 79400	1.24	238 \pm 2	9.62 \pm 0.2	7.78e-05	0.00 \pm 0.00	3.95 \pm 0.63
HIP 79439	0.69	236 \pm 0.3	56.2 \pm 1	8.27e-04	1.00 \pm 0.00	15.5 \pm 2.2
HIP 79710	1.08	245 \pm 1	4.63 \pm 0.09	3.30e-05	0.00 \pm 0.00	2.54 \pm 0.91
*HIP 79742	2.48	93.6 \pm 0.3	10.5 \pm 0.1	2.33e-02	1.00 \pm 0.00	14 \pm 2.1
HIP 79878	1.40	203 \pm 1	9.53 \pm 0.22	2.43e-04	0.00 \pm 0.00	15.9 \pm 3.6
*HIP 79977	2.54	102 \pm 0.2	11.1 \pm 0.1	4.44e-02	1.00 \pm 0.00	11.5 \pm 2.7
HIP 80024	1.70	169 \pm 0.1	10 \pm 0.04	1.81e-03	0.00 \pm 0.00	37.6 \pm 4.9
HIP 82218	1.70	154 \pm 2	9.54 \pm 0.47	2.74e-04	0.00 \pm 0.00	5.3 \pm 0.71

*Fits with formal $\chi^2_\nu > 2$ but appear to be fit well with a single-grain model by visual inspection.

Table 4. Fits to two-grain model

HIP ID	χ^2_ν	T_1 (K)	a_1 (μm)	mass ₁ (M_{moon})	$f_{o,1}$	r_1 (AU)	T_2 (K)	a_2 (μm)	mass ₂ (M_{moon})	$f_{o,2}$	r_2 (AU)
*HIP 53524	2.76	64.7 \pm 0.2	20 \pm 0.3	2.24e-01	1.00 \pm 0.00	42.2 \pm 0.2	413 \pm 23	3.32 \pm 0.56	2.86e-06	0.37 \pm 0.30	1.24 \pm 0.14
*HIP 55188	2.20	128 \pm 1	13.1 \pm 0.3	1.03e-02	1.00 \pm 0.00	13.2 \pm 0.7	535 \pm 30	3.91 \pm 0.62	4.95e-06	0.65 \pm 0.09	1.06 \pm 0.13
*HIP 58220	2.20	169 \pm 1	6.61 \pm 0.02	1.03e-04	1.00 \pm 0.00	4.1 \pm 0.39	1500 \pm 0	14.2 \pm 0.2	1.72e-06	1.00 \pm 0.00	0.068 \pm 0.006
HIP 58720	1.23	129 \pm 1	52.2 \pm 1.8	2.89e-02	0.32 \pm 0.14	35.5 \pm 4.1	468 \pm 26	6.87 \pm 1	1.49e-05	0.66 \pm 0.22	2.94 \pm 0.47
HIP 59502	1.20	104 \pm 0.4	3.62 \pm 0.002	2.67e-03	0.00 \pm 0.00	31.9 \pm 4.1	368 \pm 5	7.96 \pm 0.38	4.21e-05	0.95 \pm 0.14	1.98 \pm 0.26
*HIP 59898	2.73	153 \pm 2	7.46 \pm 0.2	1.48e-03	0.53 \pm 0.09	15.4 \pm 2.8	524 \pm 51	5.09 \pm 1	7.52e-06	0.03 \pm 0.18	1.78 \pm 0.47
[†] HIP 60183	1.34	150 \pm 3	16.1 \pm 0.7	2.65e-03	0.35 \pm 0.12	18 \pm 1.5	314 \pm 56	11 \pm 9.3	2.21e-05	1.00 \pm 0.00	4.42 \pm 1
HIP 60561	0.78	134 \pm 3	25.8 \pm 1.6	2.24e-03	1.00 \pm 0.00	16 \pm 2.8	413 \pm 24	19.2 \pm 3.8	2.48e-05	0.76 \pm 0.36	1.86 \pm 0.38
HIP 61684	0.70	106 \pm 1	14.4 \pm 0.5	6.85e-03	1.00 \pm 0.00	15.4 \pm 1.1	267 \pm 2	6.53 \pm 0.02	1.72e-05	0.00 \pm 0.00	2.41 \pm 0.18
*HIP 61782	2.86	115 \pm 0.3	13.4 \pm 0.2	2.93e-02	0.73 \pm 0.08	15.2 \pm 1.2	1500 \pm 0	4.1 \pm 0.12	2.12e-07	0.00 \pm 0.00	0.205 \pm 0.02
*HIP 62657	6.13	35.9 \pm 0.5	0.539 \pm 0.05	5.58e+00	0.00 \pm 0.00	958 \pm 172	119 \pm 1	8.03 \pm 0.54	2.08e-03	0.47 \pm 0.22	7.34 \pm 1.5
HIP 63439	1.14	69.5 \pm 0.9	15.6 \pm 1.4	3.47e-02	1.00 \pm 0.00	24.3 \pm 2.9	405 \pm 35	2.69 \pm 0.73	1.50e-06	0.66 \pm 0.36	0.951 \pm 0.2
HIP 63839	1.14	192 \pm 3	5.67 \pm 0.16	3.20e-04	0.17 \pm 0.10	7.82 \pm 0.98	753 \pm 140	4.92 \pm 2	2.26e-06	0.47 \pm 0.14	0.817 \pm 0.32
[†] HIP 63886	0.85	69.2 \pm 2	15.7 \pm 2.9	3.72e-02	1.00 \pm 0.00	28.9 \pm 7.9	292 \pm 21	6.23 \pm 1	8.30e-06	0.00 \pm 0.00	1.66 \pm 0.5
[†] HIP 64184	1.07	99 \pm 1.3	15.6 \pm 0.9	3.51e-02	0.10 \pm 0.20	11.3 \pm 0.5	140 \pm 2	2.93 \pm 0.26	5.07e-04	0.15 \pm 0.16	7.38 \pm 0.3
HIP 65875	1.45	107 \pm 1	12.5 \pm 0.4	3.30e-02	1.00 \pm 0.00	13.2 \pm 1.4	208 \pm 7	1.86 \pm 0.39	4.43e-05	0.00 \pm 0.00	4.59 \pm 0.55
HIP 65965	1.20	108 \pm 1	16.5 \pm 0.7	1.39e-02	0.90 \pm 0.15	27.4 \pm 3.2	367 \pm 12	17.1 \pm 2	5.50e-05	0.66 \pm 0.32	2.76 \pm 0.36
HIP 66068	1.51	146 \pm 4	23.8 \pm 1.9	4.08e-03	0.65 \pm 0.41	15.9 \pm 4.8	378 \pm 20	3.91 \pm 0.81	1.34e-05	0.67 \pm 0.21	2.65 \pm 0.84
HIP 66566	0.98	153 \pm 2	14.6 \pm 0.6	1.73e-03	0.52 \pm 0.20	10.8 \pm 1	428 \pm 41	4.08 \pm 1	4.22e-06	0.00 \pm 0.00	1.67 \pm 0.35
[†] HIP 67230	0.27	161 \pm 3	5.06 \pm 0.4	4.03e-04	1.00 \pm 0.00	7.55 \pm 0.84	1500 \pm 0	2.13 \pm 0.2	7.68e-08	0.00 \pm 0.00	0.213 \pm 0.02
HIP 67970	0.77	139 \pm 2	7.44 \pm 0.31	6.67e-04	0.65 \pm 0.30	6.4 \pm 0.69	1020 \pm 240	6.31 \pm 2	4.25e-07	0.82 \pm 0.24	0.188 \pm 0.09
[†] HIP 68080	1.02	157 \pm 5	23.9 \pm 2.4	2.90e-03	0.49 \pm 0.35	22.4 \pm 3.4	682 \pm 149	17.8 \pm 9.7	9.61e-06	1.00 \pm 0.00	1.47 \pm 0.68
[†] HIP 70149	0.85	108 \pm 0.5	7.64 \pm 0.01	7.01e-04	0.00 \pm 0.00	10.1 \pm 1.4	268 \pm 8	4 \pm 0.54	6.75e-06	0.00 \pm 0.00	1.66 \pm 0.26
HIP 70441	1.87	69.7 \pm 0.8	20.9 \pm 1.4	5.23e-02	1.00 \pm 0.00	46.3 \pm 5.8	268 \pm 5	3.9 \pm 0.26	1.50e-05	0.00 \pm 0.00	3.27 \pm 0.42
HIP 71271	1.13	84.6 \pm 1.4	21.9 \pm 1.9	3.69e-02	1.00 \pm 0.00	47 \pm 5.9	311 \pm 14	3.96 \pm 0.66	1.07e-05	0.00 \pm 0.00	3.74 \pm 0.56
*HIP 73145	2.24	80.4 \pm 0.3	39.1 \pm 0.7	5.60e-01	1.00 \pm 0.00	35.1 \pm 7.5	214 \pm 1	4.5 \pm 0.16	2.77e-04	0.00 \pm 0.00	4.65 \pm 1
HIP 73990	1.63	166 \pm 2	9.91 \pm 0.39	8.26e-04	1.00 \pm 0.19	6.62 \pm 0.86	1440 \pm 890	2.43 \pm 2	1.42e-07	0.46 \pm 0.23	0.173 \pm 0.22

Table 4—Continued

HIP ID	χ^2_ν	T_1 (K)	a_1 (μm)	mass ₁ (M_{moon})	$f_{o,1}$	r_1 (AU)	T_2 (K)	a_2 (μm)	mass ₂ (M_{moon})	$f_{o,2}$	r_2 (AU)
‡HIP 74499	0.75	83.7 \pm 0.8	12 \pm 0.7	7.45e-03	1.00 \pm 0.00	13.1 \pm 1.6	286 \pm 3	3.98 \pm 0.01	3.21e-06	0.00 \pm 0.00	1.14 \pm 0.14
HIP 75077	0.39	63.5 \pm 0.9	30.4 \pm 2.6	4.48e-02	0.00 \pm 0.00	79.4 \pm 14	291 \pm 14	4.08 \pm 0.63	5.61e-06	0.00 \pm 0.00	3.92 \pm 0.8
†HIP 75210	0.81	151 \pm 4	139 \pm 10	2.51e-02	0.42 \pm 0.34	26.4 \pm 3.2	477 \pm 59	4.91 \pm 1	6.10e-06	1.00 \pm 0.00	2.73 \pm 0.74
*HIP 76310	2.19	116 \pm 0.4	17 \pm 0.2	5.46e-02	1.00 \pm 0.00	52.9 \pm 5.2	361 \pm 12	10.8 \pm 1.3	6.72e-05	0.40 \pm 0.27	6.09 \pm 0.71
†HIP 77315	0.52	153 \pm 4	22.9 \pm 1.5	5.16e-03	0.26 \pm 0.28	18.4 \pm 1.8	440 \pm 48	7.23 \pm 2	1.63e-05	0.76 \pm 0.29	2.54 \pm 0.59
HIP 77317	0.88	97.3 \pm 1	54.2 \pm 3.9	6.14e-02	0.96 \pm 0.32	35 \pm 7.8	486 \pm 35	12.8 \pm 2.6	6.66e-06	0.42 \pm 0.51	1.56 \pm 0.41
HIP 78043	0.75	78.2 \pm 1.7	20.7 \pm 2.5	2.88e-02	1.00 \pm 0.00	23.1 \pm 4	307 \pm 13	6.05 \pm 0.97	9.96e-06	0.00 \pm 0.00	1.47 \pm 0.27
HIP 78641	1.54	131 \pm 1	10.5 \pm 0.4	2.47e-03	0.83 \pm 0.13	9.12 \pm 1	366 \pm 17	2.32 \pm 0.41	4.19e-06	0.06 \pm 0.12	1.5 \pm 0.32
HIP 78996	1.72	175 \pm 1	9.93 \pm 0.01	3.61e-04	1.00 \pm 0.00	14.1 \pm 2	1500 \pm 0	4.96 \pm 0.08	5.40e-07	0.71 \pm 0.09	0.306 \pm 0.04
HIP 79156	1.45	195 \pm 3	9.06 \pm 0.39	2.55e-04	1.00 \pm 0.00	18.9 \pm 2.9	1500 \pm 0	5.29 \pm 0.11	1.19e-06	0.89 \pm 0.09	0.476 \pm 0.07
HIP 79410	1.20	114 \pm 4	8.02 \pm 0.91	1.37e-03	0.00 \pm 0.00	57.5 \pm 9.9	387 \pm 9	6.71 \pm 0.51	3.65e-05	1.00 \pm 0.00	5.62 \pm 0.93
HIP 79516	1.77	72.1 \pm 1.5	24 \pm 2.6	2.51e-01	1.00 \pm 0.00	24.9 \pm 4.5	128 \pm 3	3.32 \pm 0.59	5.67e-04	0.11 \pm 0.15	9.62 \pm 1
*HIP 79631	2.33	76.8 \pm 0.8	35 \pm 0.2	2.90e-01	0.09 \pm 0.36	66 \pm 10	205 \pm 4	7.4 \pm 0.78	3.51e-04	0.00 \pm 0.00	8.78 \pm 1
‡*HIP 80088	2.86	51.7 \pm 0.4	1.55 \pm 0.11	2.45e-01	1.00 \pm 0.00	1000 \pm 140	245 \pm 3	3.4 \pm 0.17	3.10e-05	0.00 \pm 0.00	8.37 \pm 1
†HIP 80320	0.84	50.6 \pm 0.9	0.979 \pm 0.16	8.23e-02	1.00 \pm 0.00	359 \pm 68	337 \pm 18	2.34 \pm 0.43	2.74e-06	0.23 \pm 0.23	1.21 \pm 0.26
*HIP 80897	2.90	108 \pm 1	93.5 \pm 2.2	1.75e-01	1.00 \pm 0.00	30.2 \pm 5.1	481 \pm 16	36.3 \pm 3.5	6.89e-05	1.00 \pm 0.00	1.54 \pm 0.28
HIP 82154	0.86	98.3 \pm 2.5	22.3 \pm 2.2	4.74e-02	0.00 \pm 0.00	75.7 \pm 19	257 \pm 8	6.35 \pm 0.88	1.93e-04	1.00 \pm 0.00	11.1 \pm 2.9

*Fits with formal $\chi^2_\nu > 2$ but appear to be fit well with a two-grain model by visual inspection.

†Formally well-fit by a single-grain model, but appear to be better fit by a two-grain model by visual inspection.

‡IRS spectra well-fit by a two-grain model, but does not fit the 70 μm MIPS photometric value.

Table 5. Objects not fit well by single or two-grain models

HIP ID	χ^2_ν	T_1 (K)	a_1 (μm)	mass ₁ (M_{moon})	$f_{o,1}$	r_1 (AU)	T_2 (K)	a_2 (μm)	mass ₂ (M_{moon})	$f_{o,2}$	r_2 (AU)
HIP 63975											
one-grain	78.77	478 \pm 0.2	4.54 \pm 0.004	8.45e-04	1.00 \pm 0.00	2.51 \pm 0.31
two-grain	49.00	101 \pm 0.06	2.62 \pm 0.0003	8.06e-02	0.49 \pm 0.01	74.6 \pm 9.1	1110 \pm 10	2.5 \pm 0.02	6.68e-05	1.00 \pm 0.00	0.65 \pm 0.08
HIP 79288											
one-grain	793.62	361 \pm 0.1	4.38 \pm 0.01	5.49e-04	0.00 \pm 0.00	1.35 \pm 0.2
two-grain	138.68	100 \pm 0.1	2.04 \pm 0.02	4.71e-02	0.51 \pm 0.01	33.9 \pm 5.1	822 \pm 4	3.56 \pm 0.03	4.56e-05	0.48 \pm 0.00	0.418 \pm 0.06

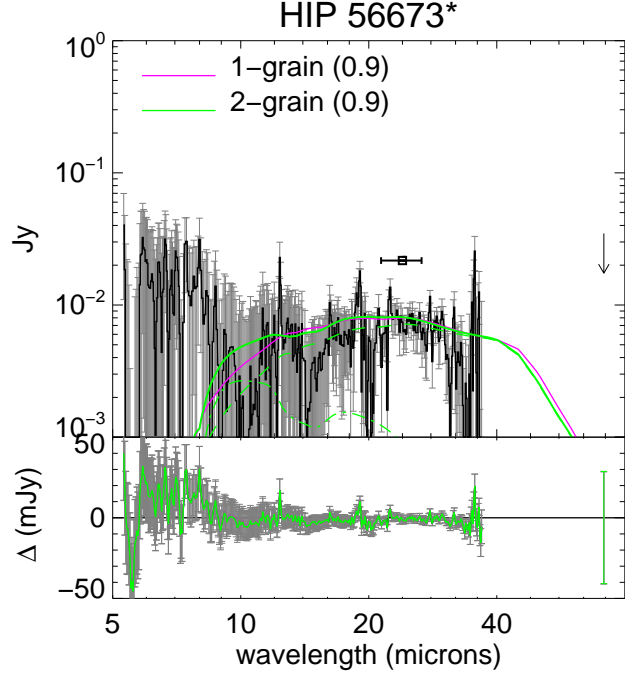


Fig. 5.— Best fitting single grain and two-grain models to HIP 56673, with the photosphere fit to the 5-6 micron region of the IRS spectrum. We find that a single component model best fits this spectrum.

This count does not include HIP 56673 or HIP 78977. As discussed previously, these sources have excesses similar to Rayleigh-Jeans profiles, consistent with either a photosphere mismatch or a hot dust component. If the photosphere is scaled to match the 5-6 micron region of the IRS spectrum, then HIP 78977 is a non-excess source, and HIP 56673 has a marginal excess that can be modeled well as a single belt. In Figure 5, we show the best fit to HIP 56673, after fitting the photosphere to the IRS spectrum instead of calibrating the photosphere to optical and near-IR photometry.

Two of our targets, HIP 63975 (HD 113766) and HIP 79288 (HD 145263) have high amounts of excess and show evidence of silicate features that cannot be adequately reproduced with the simple models used in this paper. The mineralogy of HIP 63975 was analyzed in detail in Lisse et al. (2008), and was found to consist of both amorphous and crystalline silicates, as well as Fe-rich sulfides, amorphous carbon, and water ice. HIP 79288 has a similarly complex composition, and requires silica in addition to other species to adequately model it (Lisse, et al., in prep).

HIP 74499 and HIP 80088 both appear to require at least two components to fit their IRS spectra: a large cold component to fit the 20-40 micron region, and a small hot

component to fit the 10 micron region. However, in both these cases, the best fit to the IRS spectrum does not produce enough emission at 70 micron to match the MIPS photometry. It is likely that these two systems have an additional third cold component that would account for the missing 70 micron excess. Both these sources have been classified as two-belt systems for further analysis.

Recently, a debris belt has been imaged around one of our targets, HIP 64995 (HD 115600), with a semi-major axis of ~ 48 AU. (Currie et al. 2015). Our modeling predicts a single belt of debris at a temperature of 114 K, or ~ 11 AU. This belt would be interior to the inner working angle of the coronagraphic image of the belt detected by Currie et al. (2015). If the outer belt is an analog of the Kuiper belt, then the belt predicted by the mid-infrared spectroscopy would be an asteroid belt analog. This example illustrates how mid-IR spectral analysis is complementary to coronagraphic imaging for studying the structure of debris disks.

In Figure 6, we show the masses of the dust belts in the single-belt (black) and two-belt (red/blue) debris disk systems. For the two-belt systems, the hot and cold belts are colored red and blue, respectively. Dust mass appears to be inversely correlated to temperature. This is likely a selection effect, because more cold material must exist in order for it to contribute significantly to the infrared excess. That is, a lower temperature blackbody emits less radiation total than a higher temperature one, holding the emitting surface area constant. There does not appear to be a trend in measured dust mass versus stellar mass. This implies that the trend that L_{IR}/L_* decreases with increasing stellar mass (see Figure 3) is best explained by differences in dust temperature (i.e. distance from the system primary) rather than differences in measured dust mass.

In Figure 7, we summarize the results of our models in terms of the temperatures and radial distance of the grain populations. In general, the temperatures of the single-belt models are intermediate between the hot and cold components of the two-belt models. There appears to be more scatter in the hot components for lower stellar masses, which is more easily seen in the cumulative distributions in temperature after separating them out into low mass ($\leq 1.5 M_\odot$, dashed lines) and high mass ($\geq 1.6 M_\odot$, solid lines) stars.

The same discrepancy between high-mass and low-mass stars appears in the distribution of radii of the belts, as shown in the right panel of Figure 7. The belt radii are an average distance for the olivine and pyroxene components of the grains. The model spectra assume that the olivine and pyroxene components of the dust all have the same equilibrium temperatures. The grain properties are similar enough between olivine and pyroxene that grains of the same temperature are effectively co-located as well, and the radius derived for pure olivine is nearly the same as that of pure pyroxene. Since in many cases the composition is

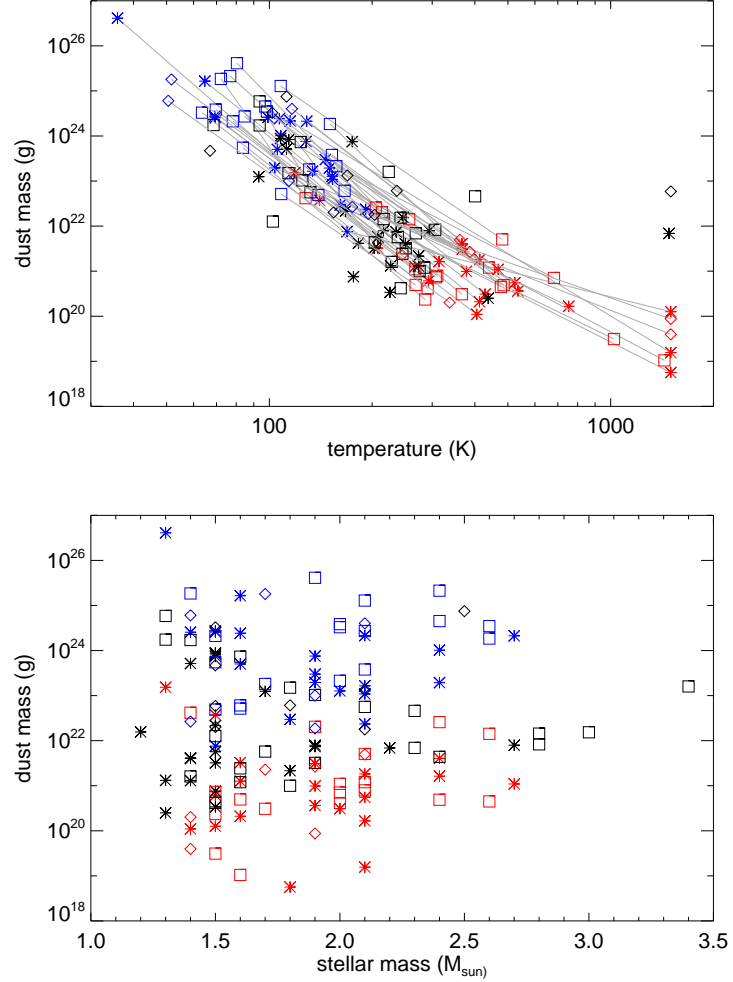


Fig. 6.— Dust belt masses versus dust temperature (top) and stellar mass (bottom), for the single grain population disks (black) and the two-grain population disks (red/blue). In the two-grain population model, the cold component is shown in blue while the hot component is shown in red. Objects belonging to LCC, UCL, and USco are labeled by asterisks, squares, and diamonds, respectively.

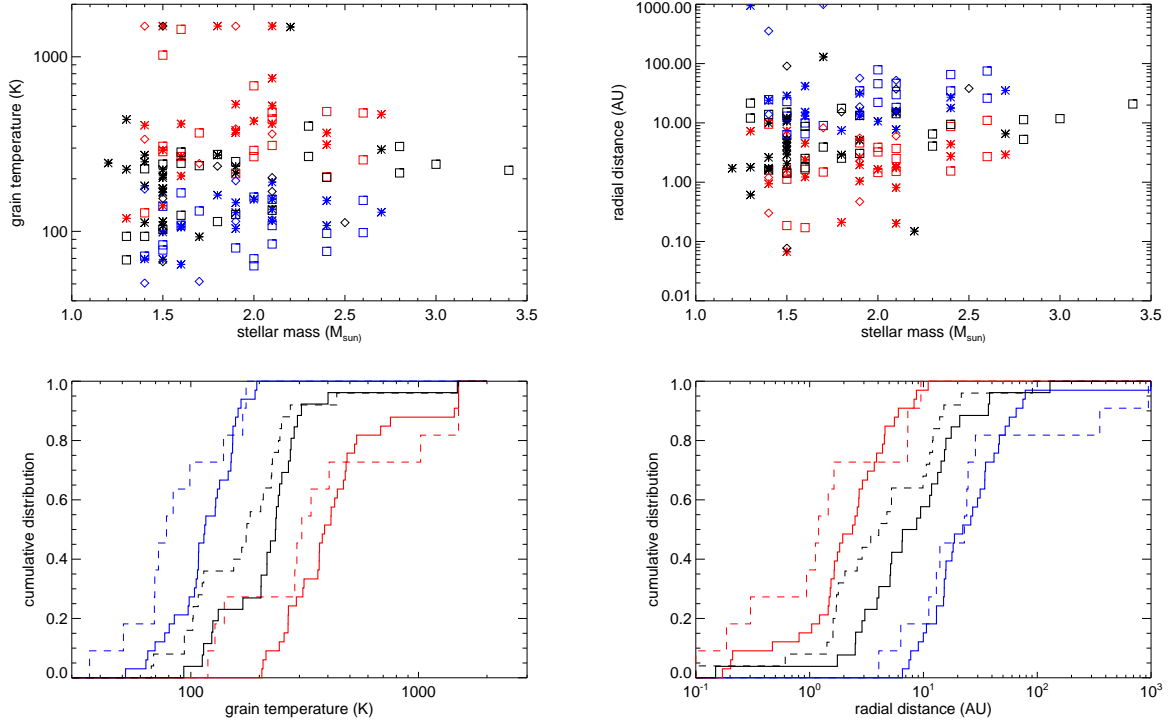


Fig. 7.— Temperature and radial distribution of grain populations in single belt (black) and two-belt (blue/red) systems. For the two-belt systems, the hot component is plotted in red, the cold component in blue. Top row: T_{gr} (left) and r (right) versus stellar mass. Objects belonging to LCC, UCL, and USco are labeled by asterisks, squares, and diamonds, respectively. Bottom row: Cumulative temperature distribution (left) and radial distribution (right) for the dust components of best fit disk models. The solid lines show stars with mass $\geq 1.6 M_{\odot}$, while the dashed lines show stars with mass $\leq 1.5 M_{\odot}$.

either pure pyroxene or pure olivine, the difference in the distances of the two components is insignificant.

The grain temperatures of dust around high mass stars are systematically higher than around low mass stars. This agrees with the finding in Chen et al. (2014). In Table 6, we show the results of the Kolmogorov-Smirnov (KS) and Anderson-Darling (AD) statistics for testing the similarity of the grain temperatures between high and low mass stars. We consider the single belt systems, the cold component of the two-belt systems, and the hot component of the two-belt systems separately. The Anderson-Darling test (Anderson & Darling 1954) is arguably a more sensitive statistic than the KS test because it gives more weight to the tails of the distributions. To test whether or not two samples X_1, \dots, X_n and Y_1, \dots, Y_m are drawn from the same populations, we can use the two-sample Anderson-Darling statistic, given by

$$A_{nm}^2 = \frac{1}{mn} \sum_{i=1}^{N-1} \frac{(M_i N - ni)^2}{i(N-i)} \quad (17)$$

where $N = m+n$ and M_i is the number of X 's less than or equal to the i th smallest element in the combined sample (Pettitt 1976).

The KS test for the single belt systems and the cold component of the two belt systems give a 10% and 4% or less probability, respectively, of being drawn from the same population, while the probability of the hot components being similar is 37%. The AD test gives comparable results: < 5% probabilities for the single belt systems and cold components, but higher probability of similarity for the hot component (> 15%). A potential explanation for this systematic shift is that higher mass stars heat the dust more than lower mass stars do, but that is not fully borne out when we examine the distributions with respect to dust distance.

It appears likely that the cold grain populations for both the high mass and low mass stars are at similar distances: the KS test gives a probability of 65% that they are drawn from the same population. However, both the single belt systems and the hot component of the two-belt systems are systematically offset to larger distances in the high mass systems, despite being hotter. The single belt systems have a 22% probability of being similar, while the probability for the hot component of the two belt systems being similar is 12%. Again, the AD test gives similar results: it is unlikely that the single belts and hot components of low mass stars are drawn from the same population as the high mass stars (< 10%). However, it is much more likely that the cold components are similar (> 15%).

The trend in L_{IR}/L_* seen in Figure 3 also supports the idea that lower mass stars have dust at closer radii. This is because the infrared excess luminosity, which is attributed to the dust, scales as $L_{IR} \propto M_d T_d^4$, where M_d and T_d are the total mass and temperature of

the dust, respectively. The temperature of the dust is determined by stellar illumination, as $T_d^4 \propto L_*/d^2$ where d is the stellocentric distance. This gives $L_{IR}/L_* \propto M_d/R^2$. If M_d stays constant, then the trend that lower mass stars have higher L_{IR}/L_* implies that the disks in lower mass stars are more compact.

This implies that that the low mass stars retain close-in dust more readily than high mass stars, suggesting that debris disks in high mass stars evolve faster than low mass stars, and that this evolution occurs inside out. One explanation for this is that debris disks evolve faster in high mass stars because the dynamical times are shorter (Kenyon & Bromley 2008). Another possibility is that the higher mass stars (F-type and earlier) evolve onto the main sequence sooner. By 15-17 Myr, the ages of LCC and UCL, these stars are already on the main sequence. The ignition of hydrogen burning in these stars could enable the clearing out of inner dust belts at $\lesssim 1$ AU. The retention of dust by low-mass stars could also simply be the result of more efficient grain blow-out by more massive stars, as indicated by their larger values of a_{\min} [Eq. (7)]. Still another possibility is that the initial protoplanetary gas disk differs between high mass and low mass stars.

5. Discussion

The high degree of scatter in the distances of the dust belts indicates that they are not likely connected to intrinsic properties of the primordial disks from which they arose. Primordial disks generally have continuous radial distributions of material rather than belts. Material could potentially pile up at pressure maxima, for example, but the origin of the pressure maxima depends on stellar properties such as effective temperature and luminosity, which should be relatively stable for a given stellar mass. An example of this phenomenon is the T Tauri object HL Tau, which has been seen to have several gaps in ALMA imagery (ALMA Partnership et al. 2015). Although it is possible that these gaps were created by planets, locations of the gaps also appear to be co-incident with condensation fronts in the disk (Zhang et al. 2015). The locations of the fronts are based on the predicted temperature profile of the disk, which in turn depends on the heating of the disk from stellar irradiation (see e.g. Kenyon & Hartmann 1987).

Alternatively, dust locations could depend on the formation of planets, which is highly stochastic in regard to stellocentric distances. The varying diameters of the inner holes seen in transitional disks are often attributed to planet formation for this reason. Planets could also explain the origin of the dust belts after the dissipation of the primordial gas, since planets could be responsible for shepherding the parent bodies that produce the dust.

Stellar companions could also affect the dust belts in our disks. A high fraction of stars in our sample have identified stellar companions. A few stars have directly imaged substellar companions that may be distant planets. Since planets and binary companions are likely to play key roles in the sculpting of debris disks, it is important to put the properties of dust belts into context with the presence of binarity and the presence of planets.

5.1. Binary Stars

A number of stars in our sample have been identified to have binary companions (Janson et al. 2013; Chen et al. 2012; Kouwenhoven et al. 2005, 2007). The projected distances of these binary companions are tabulated in Table 7. The distances are calculated from the angular separations from the above references and using Hipparcos stellar distances from van Leeuwen (2007).

Stellar companions will truncate a circumstellar disk through tidal interactions. For a debris disk, where gas has little to no dynamical effect, the disk truncation radius can be estimated from the last stable orbit. Assuming a circular orbit, the outermost radius of a circumstellar disk allowed by a binary companion can be expressed as

$$a_{\text{int}} = (0.464 - 0.380\mu)a \quad (18)$$

and the inner edge of a circumbinary disk is

$$a_{\text{ext}} = (1.60 + 4.12\mu)a \quad (19)$$

(Holman & Wiegert 1999), where μ is the ratio of the mass of the binary companion to the total masses of the two stars, and a is the semi-major axis of the binary orbit.

In Figure 8, we show the outer location of the best-fit dust belts versus the binary separation for those objects with binary companions. If the dust is best fit with a single grain population, then that distance is used. For the remaining systems, the location of the outer belt in the two-grain fit is used. We also indicate the disk truncation radius for binaries with mass ratio 0.5 (equal mass binary) and 0.1 assuming a circular orbit.

In all cases, the dust is located interior to the binary separation, so the binary companion must have truncated the disks in all these systems. A few dust belts appear close to the truncation radius of a $\mu = 0.1$ binary companion, however the projected binary separation is affected by the inclination of the system and eccentricity of the orbit, so the true truncation radius might be higher. No circumbinary dust belts in our sample of stars has been identified.

Table 6: Kolmogorov-Smirnov and Anderson-Darling tests for grain populations

population	KS test		AD test	
	D	$p(D)$	A_{mn}^2	$p(A)^\dagger$
Temperatures				
... single belt	0.33	0.097	2.5	< 0.05
... cold component	0.45	0.045	2.6	< 0.05
... hot component	0.30	0.37	1.5	> 0.15
Distances				
... single belt	0.28	0.22	2.1	< 0.10
... cold component	0.24	0.65	0.93	> 0.15
... hot component	0.39	0.12	1.9	< 0.10

[†]Based on tabulations of probabilities in Stephens (1974).

Table 7. Projected Distances of Binary Companions

HIP	HD name	a_1 (AU)	a_2 (AU)	a_3 (AU)
53524	HD 95086	440.3
58220	HD 103703	75.17
58528	HD 104231	492.8
59502	HD 106036	296.1	911.4	...
59693	HD 106389	58.49
63236	HD 112383	837.2	1326.	...
63839	HD 113457	427.4	595.4	627.2
65965	HD 117484	1514.
68080	HD 121336	268.5	3902.	...
69291	HD 123889	195.4
77315	HD 140817	100.1	5552.	...
77317	HD 140840	4126.
77520	HD 141254	223.5
78756	HD 143939	1249.
79400	HD 145357	734.2
79631	HD 145880	376.0	1132.	...
82154	HD 151109	1869.

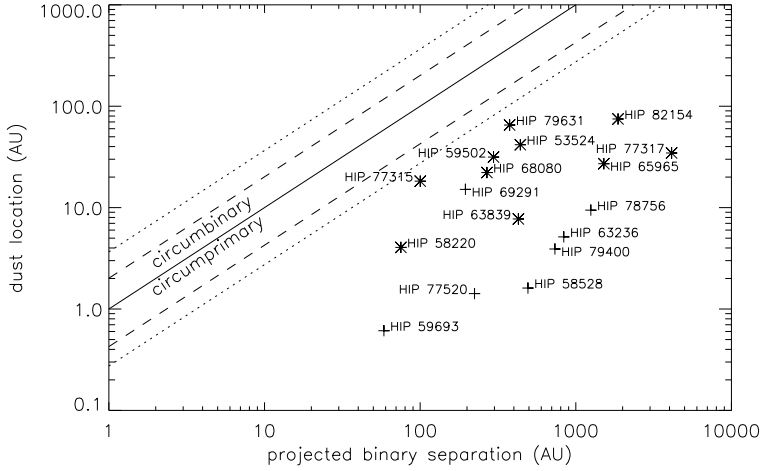


Fig. 8.— Outer dust belt location versus projected binary separation. The solid line marks the 1:1 line, so circumstellar disks lie below the solid line while circumbinary disks lie above the solid line. The dotted and dashed lines mark the disk truncation radii for an equal-mass binary and a $\mu = 0.1$ binary, respectively. Crosses indicate single belt systems, and asterisks indicate the outer belt of two-belt systems. Crosses indicate systems not well-modeled by either single or two-belt systems, but using the best fitting two-belt model regardless.

5.2. Stars with planets

Three of our sources have been identified to be planet hosts. HIP 53524 (HD 95086) is a binary star (Chen et al. 2012) around which a $\sim 5 M_{\text{Jup}}$ planet has been detected at a projected separation of 56 AU by direct imaging (Rameau et al. 2013). HIP 59960 (HD 106906) hosts a very distant planetary-mass companion at a projected separation of ~ 650 AU, also detected by direct imaging (Bailey et al. 2014). HIP 73990 (HD 133803) has at least two planets in its system, at projected separations of 20 and 32 AU (Hinkley et al. 2015).

HIP 53524 is best fit by a two-belt model, though its relatively high reduced chi-square value ($\chi^2_{\nu} = 2.8$) suggests that a few more addition parameters, such as finite belt widths or the addition of crystalline silicates, could improve the model. It hosts a stellar companion at 440 AU in addition to the imaged planet. The positions of the belts are 42 AU (65 K) and 1.2 AU (413 K), both interior to the projected position of the planet. Since the outer belt is close to the projected planet distance of 56 AU, it is likely that it is sculpted by the planet.

Herschel images of HIP 53524 marginally resolve the disk, suggesting that the systems

is surrounded by a halo that extends to around 800 AU (Su et al. 2014). That analysis included Spitzer/MIPS data and proposed that in addition to the halo, the system consists of a warm belt at 175 K and a cold belt at 55 K. The wavelength coverage of Spitzer does not provide much sensitivity to emission from the cold halo, but the 55 K belt is consistent with the model for HIP 53524 presented here. Our model predicts a hotter inner belt, which may be a result of not including the third coldest dust distribution that is inferred from the Herschel data.

In our analysis, HIP 59960 is well-fit by a single dust belt at 12 AU, and its reported planetary companion (Bailey et al. 2014) is so distant that it does not interact with the dust. It is possible that additional unseen companions exist between the belt and the planetary companion and that those companions could shepherd the dust.

HIP 73990 is best fit to a two-belt model with grain temperatures of 1440 K and 166 K, corresponding to distances of 0.17 and 6.6 AU, respectively. Assuming that planets are able to clear material out to the 2:1 mean motion resonance, then the inner planet imaged at 20 AU (Hinkley et al. 2015) should truncate the debris disk to 12.6 AU. Both dust belts detected from our spectroscopic modeling are interior to this distance.

Additional objects in ScoCen that have detected sub-stellar companions include HIP 78530, which exhibits no infrared excess; GSC 06214-00210, an accreting T Tauri star; and 1RXS J160929.1-210524. (Bailey et al. 2013). These objects were not included in our study because they are pre-main sequence stars and their disks are protoplanetary in nature.

Although imaging planets around debris disk systems can help us understand the role that planets play in sculpting debris disks, few such planet images exist. On the other hand, many debris disks are well-studied. We can turn the question around, then, and ask what can be learned about planet formation from debris disks. Dynamical interactions with planets should sculpt and shepherd debris disks. Therefore, debris disks with structure, such as gaps, can imply the presence of unseen planets.

Numerical simulations have shown that a companion orbiting in a disk can create gaps via planetesimal scattering in overlapping resonances (e.g., Roques et al. 1994; Lecavelier des Etangs et al. 1996). The width of the gap is related to the mass of the companion by a power law (e.g., Quillen 2006; Chiang et al. 2009; Rodigas et al. 2014), the parameters of which depend on the age of the system and the optical depth of the disk (Nesvold & Kuchner 2014).

Following the procedure described in Nesvold & Kuchner (2014), we analyzed the two-belt systems in our sample to place upper limits on the mass of a possible single perturbing companion in each system. In each case, we assumed that a single body on a circular orbit equidistant in log semimajor axis between the two dust bands has cleared the gap between

the bands. We used L_{IR}/L_\star as a proxy for the face-on optical depth of each disk.

Nesvold & Kuchner (2014) found that the largest gap size that a single body on a circular orbit can create has a full width of $\Delta r/r = 1.6$. Larger bodies tend to stir the disk; destroying it and widening it, while roughly preserving the gap edge near the location of the 2:1 mean motion resonance. Nine disks in our sample had gaps narrower than this maximum width. Table (8) summarizes inferred companion masses and semimajor axes for these nine disks.

Five of these systems, HIP 61684, HIP 66068, HIP 78641, HIP 65875, and HIP 79516, have small enough gaps that they require a single perturbing body whose mass is in the range of planet masses. The other disks require either planets on eccentric orbits, companions in the brown-dwarf mass range or multiple planets. The inferred companions in these systems are all located within 0.2 arcseconds of their host stars, probably too close to detect directly with today’s instruments. However, future observatories, such as WFIRST-AFTA, may be able to resolve sub-stellar companions at angular separations of less than $0.2''$. In addition, the next generation of large aperture ground-based telescopes, such as GMT, TMT, or E-ELT, could have the necessary resolving power and inner working angle. ATLAST, currently a NASA strategic mission concept study, could also detect these planets.

HIP 82154 also has a binary companion at a projected distance of 1869 AU (see Table 8). This companion is probably too distant to have any dynamical effect on the dust belts or any planet located between them.

Six out of the nine inferred companions listed in Table (8) have estimated semimajor axes within 5 ± 3 AU, close to Jupiter’s semi-major axis of 5.2 AU. This lends credence to the idea that giant planets preferentially form in the 5-10 AU range. This is also consistent

Table 8: Masses and semimajor axes of companions inferred from the disk gaps.

HIP	Companion	Semimajor Axis (AU)	Max Companion Mass (M_{Jup})
60561		5.4	28.8
61684		6.4	12.2
65089		22.9	33.1
66068		5.9	10.4
66566		4.2	15.3
78641		3.7	9.8
82154		28.7	42.9
65875		7.7	1.1
79516		15.3	0.8

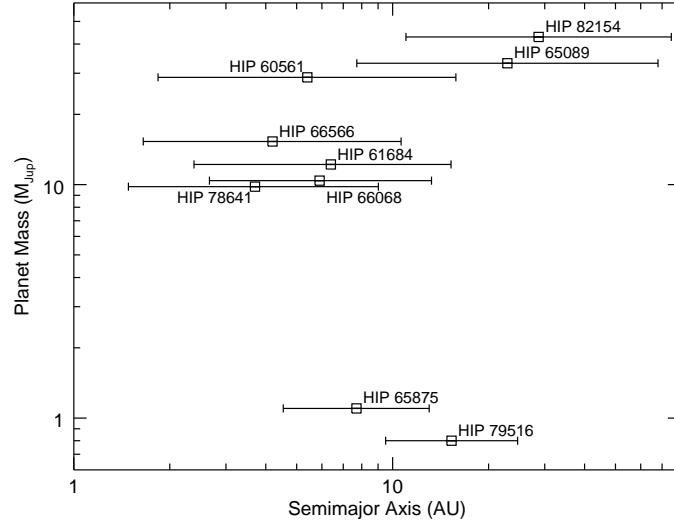


Fig. 9.— Maximum companion mass vs. estimated companion semimajor axis for the nine companions inferred from the disk gaps. The bars indicate the widths of the gaps between belts.

with statistics of exoplanets showing that, apart from hot Jupiters, the number of exoplanets increases toward orbital separations larger than 1 AU.

6. Conclusions

Constraining our study of debris disks to those in ScoCen gives us the advantage of examining a cohort of debris disks of similarly young age. Within this sample, we find evidence of mass-dependent evolution of the hot dust. In particular, in systems with two belts, low mass stars have closer inner belts than high mass stars. This implies that high mass stars have less hot dust than low mass stars. This could be related to the faster evolution times of the higher mass stars, which results in higher mass stars reaching the main sequence sooner than the less massive stars. Then the lack of hot dust could be explained by the clearing of the dust from the inside out as the star evolves.

We explored how stellar and sub-stellar companions could sculpt debris disks. Many of the objects in our sample have known binary companions. We find that the dust distances from our models predict circumstellar disks rather than circumbinary disks. However, because the binaries are generally wide, and our data is limited to infrared wavelengths, our observations are not sensitive to any thermal emission that might come from circumbinary disks. The dust distances are consistent with disk truncation at outer radii by the binary companion.

Two of our objects host known planets. These planets have been detected by direct imaging, so they are distant planets outside the dust disks. The fact that the planets that have been discovered in ScoCen also host debris disks suggest that debris disks and planet formation are correlated. Planets can also sculpt debris disks, and we use this fact to consider the possibility that our disks might host planets.

The locations of dust belts can put constraints on the locations of planets since they should clear out gaps in the disks. The two-belt systems found in our study could be the result of one or several planets carving out gaps. If the distance ratios are small, then the location and mass of the potential planet can be narrowly constrained. These systems are particularly good targets for follow-up planet searches.

Wider gaps could be created by multiple planets or eccentric orbits. These are also good targets for follow-up, although predictions about planet properties are less well-constrained.

This work is based on observations made with the Spitzer Space Telescope, which is operated by JPL/Caltech under a contract with NASA. Support for this work was provided by NASA through an award issued by JPL/Caltech. HJ-C acknowledges support from NASA grant NNX12AD43G.

REFERENCES

ALMA Partnership, Brogan, C. L., Perez, L. M., Hunter, T. R., Dent, W. R. F., Hales, A. S., Hills, R., Corder, S., Fomalont, E. B., Vlahakis, C., Asaki, Y., Barkats, D., Hirota, A., Hodge, J. A., Impellizzeri, C. M. V., Kneissl, R., Liuzzo, E., Lucas, R., Marcelino, N., Matsushita, S., Nakanishi, K., Phillips, N., Richards, A. M. S., Toledo, I., Aladro, R., Broguiere, D., Cortes, J. R., Cortes, P. C., Espada, D., Galarza, F., Garcia-Appadoo, D., Guzman-Ramirez, L., Humphreys, E. M., Jung, T., Kamen, S., Laing, R. A., Leon, S., Marconi, G., Mignano, A., Nikolic, B., Nyman, L.-A., Radiszc, M., Remijan, A., Rodon, J. A., Sawada, T., Takahashi, S., Tilanus, R. P. J., Vila Vilaro, B., Watson, L. C., Wiklind, T., Akiyama, E., Chapillon, E., de Gregorio-Monsalvo, I., Di Francesco, J., Gueth, F., Kawamura, A., Lee, C.-F., Nguyen Luong, Q., Mangum, J., Pietu, V., Sanhueza, P., Saigo, K., Takakuwa, S., Ubach, C., van Kempen, T., Wootten, A., Castro-Carrizo, A., Francke, H., Gallardo, J., Garcia, J., Gonzalez, S., Hill, T., Kaminski, T., Kurono, Y., Liu, H.-Y., Lopez, C., Morales, F., Plarre, K., Schieven, G., Testi, L., Videla, L., Villard, E., Andreani, P., Hibbard, J. E., & Tatematsu, K. 2015, ArXiv e-prints

Anderson, T. W. & Darling, D. A. 1954, Journal of the American Statistical Association, 49, pp. 765

Artymowicz, P. 1988, ApJ, 335, L79

Aumann, H. H. 1984, in Bulletin of the American Astronomical Society, Vol. 16, Bulletin of the American Astronomical Society, 483

Backman, D. E. & Paresce, F. 1993, in Protostars and Planets III, ed. E. H. Levy & J. I. Lunine, 1253–1304

Bailey, V., Hinz, P. M., Currie, T., Su, K. Y. L., Esposito, S., Hill, J. M., Hoffmann, W. F., Jones, T., Kim, J., Leisenring, J., Meyer, M., Murray-Clay, R., Nelson, M. J., Pinna, E., Puglisi, A., Rieke, G., Rodigas, T., Skemer, A., Skrutskie, M. F., Vaitheeswaran, V., & Wilson, J. C. 2013, ApJ, 767, 31

Bailey, V., Meshkat, T., Reiter, M., Morzinski, K., Males, J., Su, K. Y. L., Hinz, P. M., Kenworthy, M., Stark, D., Mamajek, E., Briguglio, R., Close, L. M., Follette, K. B., Puglisi, A., Rodigas, T., Weinberger, A. J., & Xompero, M. 2014, ApJ, 780, L4

Bitner, M. A., Chen, C. H., Muzerolle, J., Weinberger, A. J., Pecaut, M., Mamajek, E. E., & McClure, M. K. 2010, ApJ, 714, 1542

Cannon, A. J. & Pickering, E. C. 1920, Annals of Harvard College Observatory, 95, 1

Carpenter, J. M., Bouwman, J., Mamajek, E. E., Meyer, M. R., Hillenbrand, L. A., Backman, D. E., Henning, T., Hines, D. C., Hollenbach, D., Kim, J. S., Moro-Martin, A., Pascucci, I., Silverstone, M. D., Stauffer, J. R., & Wolf, S. 2009a, *ApJS*, 181, 197

Carpenter, J. M., Bouwman, J., Silverstone, M. D., Kim, J. S., Stauffer, J., Cohen, M., Hines, D. C., Meyer, M. R., & Crockett, N. 2008, *ApJS*, 179, 423

Carpenter, J. M., Mamajek, E. E., Hillenbrand, L. A., & Meyer, M. R. 2009b, *ApJ*, 705, 1646

Chen, C. H., Li, A., Bohac, C., Kim, K. H., Watson, D. M., van Cleve, J., Houck, J., Stapelfeldt, K., Werner, M. W., Rieke, G., Su, K., Marengo, M., Backman, D., Beichman, C., & Fazio, G. 2007, *ApJ*, 666, 466

Chen, C. H., Mamajek, E. E., Bitner, M. A., Pecaut, M., Su, K. Y. L., & Weinberger, A. J. 2011, *ApJ*, 738, 122

Chen, C. H., Mittal, T., Kuchner, M., Forrest, W. J., Lisse, C. M., Manoj, P., Sargent, B. A., & Watson, D. M. 2014, *ApJS*, 211, 25

Chen, C. H., Pecaut, M., Mamajek, E. E., Su, K. Y. L., & Bitner, M. 2012, *ApJ*, 756, 133

Chen, C. H., Sheehan, P., Watson, D. M., Manoj, P., & Najita, J. R. 2009, *ApJ*, 701, 1367

Chiang, E. I., Kite, E. S., Kalas, P., Graham, J. R., & Clampin, M. 2009, *ApJ*, 693, 734

Corbally, C. J. 1984, *ApJS*, 55, 657

Currie, T., Lisse, C. M., Kuchner, M. J., Madhusudhan, N., Kenyon, S. J., Thalmann, C., Carson, J., & Debes, J. H. 2015, ArXiv e-prints

Dahm, S. E. & Carpenter, J. M. 2009, *AJ*, 137, 4024

de Zeeuw, P. T., Hoogerwerf, R., de Bruijne, J. H. J., Brown, A. G. A., & Blaauw, A. 1999, *AJ*, 117, 354

Dorschner, J., Begemann, B., Henning, T., Jaeger, C., & Mutschke, H. 1995, *A&A*, 300, 503

Draine, B. T. & Lee, H. M. 1984, *ApJ*, 285, 89

Engelbracht, C. W., Blaylock, M., Su, K. Y. L., Rho, J., Rieke, G. H., Muzerolle, J., Padgett, D. L., Hines, D. C., Gordon, K. D., Fadda, D., Noriega-Crespo, A., Kelly, D. M., Latter, W. B., Hinz, J. L., Misselt, K. A., Morrison, J. E., Stansberry, J. A., Shupe, D. L., Stolovy, S., Wheaton, W. A., Young, E. T., Neugebauer, G., Wachter, S., Pérez-González, P. G., Frayer, D. T., & Marleau, F. R. 2007, *PASP*, 119, 994

Gahm, G. F., Ahlin, P., & Lindroos, K. P. 1983, *A&AS*, 51, 143

Glaspey, J. W. 1972, *AJ*, 77, 474

Hiltner, W. A., Garrison, R. F., & Schild, R. E. 1969, *ApJ*, 157, 313

Hinkley, S., Kraus, A. L., Ireland, M. J., Cheetham, A., Carpenter, J. M., Tuthill, P., Lacour, S., Evans, T. M., & Haubois, X. 2015, ArXiv e-prints

Holman, M. J. & Wiegert, P. A. 1999, *AJ*, 117, 621

Houk, N. 1978, Michigan Catalogue of Two-dimensional Spectral Types for the HD stars. Volume II. (Ann Arbor, MI: Univ. of Michigan)

—. 1982, Michigan Catalogue of Two-dimensional Spectral Types for the HD stars. Volume 3. (Ann Arbor, MI: Univ. of Michigan)

Houk, N. & Cowley, A. P. 1975, University of Michigan Catalogue of Two-dimensional Spectral Types for the HD stars. Volume I. (Ann Arbor, MI: Univ. of Michigan)

Houk, N. & Smith-Moore, M. 1988, Michigan Catalogue of Two-dimensional Spectral Types for the HD Stars. Volume 4. (Ann Arbor, MI: Univ. of Michigan)

Hube, D. P. 1970, *MmRAS*, 72, 233

Jaeger, C., Mutschke, H., Begemann, B., Dorschner, J., & Henning, T. 1994, *A&A*, 292, 641

Janson, M., Lafrenière, D., Jayawardhana, R., Bonavita, M., Girard, J. H., Brandeker, A., & Gizis, J. E. 2013, *ApJ*, 773, 170

Kenyon, S. J. & Bromley, B. C. 2004, *AJ*, 127, 513

—. 2008, *ApJS*, 179, 451

Kenyon, S. J. & Hartmann, L. 1987, *ApJ*, 323, 714

Köhler, R., Kunkel, M., Leinert, C., & Zinnecker, H. 2000, *A&A*, 356, 541

Kolokolova, L., Jockers, K., Gustafson, B. Å. S., & Lichtenberg, G. 2001, *J. Geophys. Res.*, 106, 10113

Kolokolova, L., Kimura, H., Kiselev, N., & Rosenbush, V. 2007, *A&A*, 463, 1189

Kouwenhoven, M. B. N., Brown, A. G. A., Portegies Zwart, S. F., & Kaper, L. 2007, *A&A*, 474, 77

Kouwenhoven, M. B. N., Brown, A. G. A., Zinnecker, H., Kaper, L., & Portegies Zwart, S. F. 2005, *A&A*, 430, 137

Kunkel, M. 1999, PhD thesis, Julius-Maximilians-Universität Würzburg

Kurucz, R. L. 1979, *ApJS*, 40, 1

Lagrange, A.-M., Bonnefoy, M., Chauvin, G., Apai, D., Ehrenreich, D., Boccaletti, A., Gratadour, D., Rouan, D., Mouillet, D., Lacour, S., & Kasper, M. 2010, *Science*, 329, 57

Lebouteiller, V., Barry, D. J., Spoon, H. W. W., Bernard-Salas, J., Sloan, G. C., Houck, J. R., & Weedman, D. W. 2011, *ApJS*, 196, 8

Lecavelier des Etangs, A., Scholl, H., Roques, F., Sicardy, B., & Vidal-Madjar, A. 1996, *Icarus*, 123, 168

Lisse, C. M., A'Hearn, M. F., Hauser, M. G., Kelsall, T., Lien, D. J., Moseley, S. H., Reach, W. T., & Silverberg, R. F. 1998, *ApJ*, 496, 971

Lisse, C. M., Chen, C. H., Wyatt, M. C., & Morlok, A. 2008, *ApJ*, 673, 1106

Macintosh, B., Graham, J. R., Ingraham, P., Konopacky, Q., Marois, C., Perrin, M., Poyneer, L., Bauman, B., Barman, T., Burrows, A., Cardwell, A., Chilcote, J., De Rosa, R. J., Dillon, D., Doyon, R., Dunn, J., Erikson, D., Fitzgerald, M., Gavel, D., Goodsell, S., Hartung, M., Hibon, P., Kalas, P. G., Larkin, J., Maire, J., Marchis, F., Marley, M., McBride, J., Millar-Blanchaer, M., Morzinski, K., Norton, A., Oppenheimer, B. R., Palmer, D., Patience, J., Pueyo, L., Rantakyro, F., Sadakuni, N., Saddlemyer, L., Savransky, D., Serio, A., Soummer, R., Sivaramakrishnan, A., Song, I., Thomas, S., Wallace, J. K., Wiktorowicz, S., & Wolff, S. 2014, ArXiv e-prints

Mamajek, E. E., Meyer, M. R., & Liebert, J. 2002, *AJ*, 124, 1670

Manoj, P., Bhatt, H. C., Maheswar, G., & Muneer, S. 2006, *ApJ*, 653, 657

Marley, M. S., Fortney, J. J., Hubickyj, O., Bodenheimer, P., & Lissauer, J. J. 2007, *ApJ*, 655, 541

Marois, C., Zuckerman, B., Konopacky, Q. M., Macintosh, B., & Barman, T. 2010, *Nature*, 468, 1080

Martín, E. L. 1998, *AJ*, 115, 351

Meng, H. Y. A., Su, K. Y. L., Rieke, G. H., Stevenson, D. J., Plavchan, P., Rujopakarn, W., Lisse, C. M., Poshyachinda, S., & Reichart, D. E. 2014, *Science*, 345, 1032

Morgan, W. W., Abt, H. A., & Tapscott, J. W. 1978, Revised MK Spectral Atlas for stars earlier than the sun (Williams Bay: Yerkes Observatory, and Tucson: Kitt Peak National Observatory)

Nesvold, E. R. & Kuchner, M. J. 2014, *ApJ*, submitted

Okamoto, Y. K., Kataza, H., Honda, M., Yamashita, T., Onaka, T., Watanabe, J.-i., Miyata, T., Sako, S., Fujiyoshi, T., & Sakon, I. 2004, *Nature*, 431, 660

Pecaut, M. J., Mamajek, E. E., & Bubar, E. J. 2012, *ApJ*, 746, 154

Pettitt, A. N. 1976, *Biometrika*, 63, 161

Preibisch, T., Brown, A. G. A., Bridges, T., Guenther, E., & Zinnecker, H. 2002, *AJ*, 124, 404

Preibisch, T., Guenther, E., Zinnecker, H., Sterzik, M., Frink, S., & Roeser, S. 1998, *A&A*, 333, 619

Preibisch, T. & Mamajek, E. 2008, The Nearest OB Association: Scorpius-Centaurus (Sco OB2), ed. Reipurth, B., 235

Preibisch, T. & Zinnecker, H. 1999, *AJ*, 117, 2381

Quillen, A. C. 2006, *MNRAS*, 372, L14

Rameau, J., Chauvin, G., Lagrange, A.-M., Meshkat, T., Boccaletti, A., Quanz, S. P., Currie, T., Mawet, D., Girard, J. H., Bonnefoy, M., & Kenworthy, M. 2013, *ApJ*, 779, L26

Rodigas, T. J., Malhotra, R., & Hinz, P. M. 2014, *ApJ*, 780, 65

Roques, F., Scholl, H., Sicardy, B., & Smith, B. A. 1994, *Icarus*, 108, 37

Schild, R. E., Neugebauer, G., & Westphal, J. A. 1971, *AJ*, 76, 237

Slesnick, C. L., Carpenter, J. M., & Hillenbrand, L. A. 2006, *AJ*, 131, 3016

Stephens, M. A. 1974, *Journal of the American Statistical Association*, 69, pp. 730

Sturm, B., Bouwman, J., Henning, T., Evans, N. J., Waters, L. B. F. M., van Dishoeck, E. F., Green, J. D., Olofsson, J., Meeus, G., Maaskant, K., Dominik, C., Augereau, J. C., Mulders, G. D., Acke, B., Merin, B., & Herczeg, G. J. 2013, *A&A*, 553, A5

Su, K. Y., Morrison, S. J., Malhotra, R., Balog, Z., & Smith, P. S. 2014, in AAS/Division for Planetary Sciences Meeting Abstracts, Vol. 46, AAS/Division for Planetary Sciences Meeting Abstracts, #204.02

Su, K. Y. L., Rieke, G. H., Stansberry, J. A., Bryden, G., Stapelfeldt, K. R., Trilling, D. E., Muzerolle, J., Beichman, C. A., Moro-Martin, A., Hines, D. C., & Werner, M. W. 2006, *ApJ*, 653, 675

Su, K. Y. L., Rieke, G. H., Stapelfeldt, K. R., Malhotra, R., Bryden, G., Smith, P. S., Misselt, K. A., Moro-Martin, A., & Williams, J. P. 2009, *ApJ*, 705, 314

Torres, C. A. O., Quast, G. R., da Silva, L., de La Reza, R., Melo, C. H. F., & Sterzik, M. 2006, *A&A*, 460, 695

van Leeuwen, F., ed. 2007, *Astrophysics and Space Science Library*, Vol. 350, Hipparcos, the New Reduction of the Raw Data

Vieira, S. L. A., Corradi, W. J. B., Alencar, S. H. P., Mendes, L. T. S., Torres, C. A. O., Quast, G. R., Guimarães, M. M., & da Silva, L. 2003, *AJ*, 126, 2971

Walter, F. M., Vrba, F. J., Mathieu, R. D., Brown, A., & Myers, P. C. 1994, *AJ*, 107, 692

Wilner, D. J., Andrews, S. M., & Hughes, A. M. 2011, *ApJ*, 727, L42

Zhang, K., Blake, G. A., & Bergin, E. A. 2015, ArXiv e-prints